

# A conservative, implicit solver for 0D-2V multi-species nonlinear Fokker-Planck collision equations

Yanpeng Wang<sup>a</sup>, Jianyuan Xiao<sup>1a</sup>, Yifeng Zheng<sup>c</sup>, Zhihui Zou<sup>d</sup>, Pengfei Zhang<sup>b</sup>, Ge Zhuang<sup>a</sup>

<sup>a</sup>School of Nuclear Sciences and Technology, University of Science and Technology of China, Hefei, 230026, China

<sup>b</sup>School of Physical Sciences, University of Science and Technology of China, Hefei, 230026, China

<sup>c</sup>Institute of Plasma Physics, Chinese Academy of Sciences, Hefei 230031, China

<sup>d</sup>Institute for Fusion Theory and Simulation, School of Physics, Zhejiang University, Hangzhou 310027, China

**Abstract.** In this study, we present an optimal implicit algorithm specifically designed to accurately solve the multi-species nonlinear 0D-2V axisymmetric Fokker-Planck-Rosenbluth (FPR) collision equation while preserving mass, momentum, and energy. Our approach relies on the utilization of nonlinear Shkarofsky's formula of FPR (FPRS) collision operator in terms of Legendre polynomial expansions. The key innovation lies in the introduction of a new function named King (Eq. (54)), with the adoption of the Legendre polynomial expansion for the angular direction and King function expansion for the velocity axis direction. The Legendre polynomial expansion will converge exponentially and the King method, a moment convergence algorithm, could ensure the conservation with high precision in discrete form. Additionally, post-step projection to manifolds is employed to enforce symmetries of the collision operators exactly. Through solving several typical problems across various nonequilibrium configurations, we demonstrate the high accuracy and superior performance of our algorithm.

**Keywords:** Fokker-Planck-Rosenbluth, Conservation, Nonlinear, Meshfree, Legendre polynomial, King function.

## 1 Introduction

In plasma physics, the Fokker-Planck collision operator, known as the Fokker-Planck-Rosenbluth<sup>1-4</sup> (FPR) or equivalently the Fokker-Planck-Landau<sup>5</sup> (FPL) operator, is a fundamental tool for describing Coulomb collisions between particles under the assumptions of binary, grazing-angle collisions. This operator is particularly valuable for modeling various plasma systems, including those found in laboratory settings such as magnetic confinement fusion (MCF) and inertial confinement fusion (ICF), as well as in natural environments like Earth's magnetosphere and astrophysical phenomena like solar coronal plasma. When coupled with Vlasov's equation<sup>6</sup> and Maxwell's equations, it provides a comprehensive description of weakly coupled plasma across all collisionality regimes.

The FPR collision operator ensures strict conservation of mass, momentum and energy, while also adhering to the well-established H-theorem<sup>7</sup>, which guarantees that the entropy of the plasma system increases monotonically with time unless the system reaches a thermal equilibrium state. Throughout history, various formulations of the Fokker-Planck collision operator have been developed to suit different computational and theoretical needs. The FPL collision operator employs a direct integral formulation, making it ideal for conservative algorithms and the H-theorem<sup>7</sup> due to its symmetric nature. Conversely, the standard FPR collision operator<sup>1</sup> represents integral relationships using Rosenbluth potentials, which satisfies the Poisson equation in velocity space. The

---

<sup>1</sup>xiaojy@ustc.edu.cn

divergence form of the FPR (FPRD)<sup>2,8,9</sup> collision operator is widely favored in numerical simulations due to its efficiency in fast solvers. Additionally, when employing spherical harmonic expansions, Shkarofsky's formula of the FPR collision operator (FPRS)<sup>3,4</sup> collision operator is often preferred for its computational advantages. These various formulations offer flexibility and efficiency in solving Vlasov-Fokker-Planck (VFP) equation, catering to different computational and theoretical requirements.

Historically, numerous efforts have been dedicated to addressing the numerical solution of the Fokker-Planck collision equation. Thomas<sup>10</sup> and Bell<sup>11</sup> reviewed the different numerical models of Fokker-Planck collision operator for ICF plasma. Cartesian tensor expansions<sup>12-15</sup> (CTE) and spherical harmonic expansions<sup>11,16-20</sup> (SHE), or Legendre polynomial expansions<sup>21-26</sup> when axisymmetric, are employed to handle the Fokker-Planck collision operator, which are considered equivalent to each other<sup>12</sup>.

SHE<sup>11,17,22-25</sup> is an crucial method for moderate nonequilibrium plasma when the ratio of average velocity to thermal velocity is not large. As emphasized by Bell<sup>11</sup>, the amplitude of each harmonics will decay exponentially at a rate proportional to  $l(l+1)/2$ . Even in cases of weak collisions, this  $l(l+1)/2$  leads to strong damping of higher-order spherical harmonics, naturally terminating the expansion. Early studies by Bell<sup>22</sup> and Matte<sup>23</sup> focused on including the first two order harmonics to investigate non-Spitzer heat flow in ICF plasma. Subsequent work by Shkarofsky<sup>24</sup> and Alouani-Bibi<sup>25</sup> extended this approach to higher orders, resulting in the widely used semi-anisotropic collision operator<sup>25</sup>. In recent years, several VFP codes<sup>11,17,27</sup> based on the semi-anisotropic model have been developed. However, effectively calculating the full nonlinear collision operator in the SHE approach remains a challenge<sup>11,17</sup>, especially in scenarios involving large mass disparities such as electron-deuterium collisions in fusion plasma. While previous simulations utilizing SHE have adopted the semi-anisotropic model and maintained mass and energy conservation, achieving exact momentum conservation in discrete simulations remains problematic.

Other computational approaches such as meshfree methods<sup>28-31</sup> and finite volume method<sup>32</sup> (FVM) are also employed to solve the Fokker-Planck collision equation. Fast spectral method based on FFT<sup>28-30</sup> or Hermite polynomial expansion<sup>33</sup> has shown rapid convergence of spectral expansion strategy<sup>34</sup> in approximating the FPL collision operator. Additionally, Askari<sup>31</sup> employed a meshfree method using multi-quadric radial basis functions (RBFs) to approximate the solution of the 0D-1V Fokker-Planck collision equation. Taitano et. al.<sup>2,9,35-37</sup> carried out systematic studies based on the 0D-2V FPRD collision operator by directly discretizing the collision equation with FVM. They<sup>2</sup> developed a implicit algorithm and overcame the Courant-Friedrichs-Lewy<sup>38</sup> (CFL) condition by utilizing a second-order BDF2 implicit solver and employing the multigrid (MG) method<sup>39</sup> in Jacobian-Free Newton-Krylov (JFNK)<sup>39</sup> solver. Furthermore, by normalizing the velocity space to the local thermal velocities of each species individually<sup>40</sup>, works in Ref.<sup>9</sup> developed a discrete conservation strategy that utilizes nonlinear constraints to enforce the continuum symmetries of the collision operator. However, those approaches did not take advantages of Coulomb collisions, similar to SHE<sup>11</sup>, to reduce the number of meshgrids when there are no distinguishing asymmetries in the velocity space.

The challenge of employing SHE<sup>11</sup> and previous meshfree<sup>31</sup> approaches lies in embedding discrete conservation laws within the numerical scheme. According to manifold theory<sup>41</sup>, maintaining a small local error through post-step projection to manifolds preserves the same convergence rate. Therefore, backward error analysis<sup>42,43</sup> has become a

crucial tool for understanding the long-term behavior of numerical integration methods and preserving conservation properties in the numerical scheme.

In this study, our objective is to address the full nonlinearity, discrete conservation laws, and the temporal stiffness challenge of the 0D-2V axisymmetric multi-species FPRS collision equation within the SHE approach. Similar to previous works in Ref.<sup>9</sup>, we normalize the velocity spaces to the local thermal velocities for all species separately. However, instead of utilizing multigrid (MG) technology as in Ref.<sup>2</sup>, we employ a meshfree<sup>44</sup> approach based on King method (details in Sec. 3.2.1) by introducing a novel shape function named King to overcome the classical CFL condition. To tackle the nonlinear, stiff FPRS collision equations, we propose an implicit algorithm based on Legendre polynomial expansion for the angular direction, the King function expansion for the velocity axis direction, and the trapezoidal method<sup>34,45</sup> for time integration. Romberg integration<sup>46</sup> is employed to compute kinetic moments with high precision, and backward error analysis<sup>42,43,47</sup> is applied to ensure numerical conservation of mass, momentum, and energy. The H-theorem<sup>7</sup> will be satisfied in the discretization scheme and utilized as a criterion for convergence of our algorithm.

The rest of this paper is organized as follows. Sec.2 introduces the FPRS collision equation and its normalization. The discretization of the nonlinear FPRS collision equation is given in Sec.3, encompassing angular discretization and the King method for the velocity axis dimension. An implicit time discretization and conservation strategies is discussed in Sec.4. The numerical performance of our solver, including accuracy and efficiency, is demonstrated with various multi-species tests in Sec.5. Finally, we conclude our work in Sec.6.

## 2 The Fokker-Planck-Rosenbluth collision equation

The relaxation of coulomb collision in a spatially homogeneous multi-species plasma can be described by the FPR collision equation for the velocity distribution functions of species  $a$ ,  $f(\mathbf{v}, t)$ , in velocity space  $\mathbf{v}$ :

$$\frac{\partial}{\partial t} f = \mathfrak{C}(\mathbf{v}, t) . \quad (1)$$

The term on the right-hand side is total FPR collision operator of species  $a$ , given by:

$$\mathfrak{C}(\mathbf{v}, t) = \sum_{b=1}^{N_s} \mathfrak{C}_{ab} . \quad (2)$$

Here,  $N_s$  represents the total number of plasma species and function  $\mathfrak{C}_{ab}$  denotes the FPRS collision operator for species  $a$  colliding with species  $b$ <sup>3,4</sup>, reads:

$$\mathfrak{C}_{ab}(\mathbf{v}, t) = \Gamma_{ab} \left[ 4\pi m_M F f + (1 - m_M) \nabla_{\mathbf{v}} H \cdot \nabla_{\mathbf{v}} f + \frac{1}{2} \nabla_{\mathbf{v}} \nabla_{\mathbf{v}} G : \nabla_{\mathbf{v}} \nabla_{\mathbf{v}} f \right] . \quad (3)$$

In this equation,  $\Gamma_{ab} = 4\pi \left( \frac{q_a q_b}{4\pi \varepsilon_0 m_a} \right)^2 \ln \Lambda_{ab}$ ,  $m_M = m_a/m_b$ ,  $m_a$  and  $m_b$  are the masses of species  $a$  and  $b$  respectively,  $q_a$  and  $q_b$  are the charges of species  $a$  and  $b$ . The parameters  $\varepsilon_0$  and  $\ln \Lambda_{ab}$  represent the permittivity constant of vacuum and the Coulomb logarithm<sup>48</sup> of species  $a$  and  $b$  which is a weak function of the number of particles in the Debye sphere, the identity  $\overleftrightarrow{A} \mathbf{x} : \overleftrightarrow{B} \mathbf{y} = (\mathbf{x} \cdot \overleftrightarrow{B})(\overleftrightarrow{A} \cdot \mathbf{y})$  where  $\overleftrightarrow{A}$  is a tensor. Function  $F = F(\mathbf{v}_b, t)$

represents the distribution function of background species  $b$ . Functions  $H$  and  $G$  represent Rosenbluth potentials, which are integral operators for the background distribution function  $F$ , reads:

$$H(\mathbf{v}) = \int \frac{1}{|\mathbf{v} - \mathbf{v}_b|} F(\mathbf{v}_b, t) d\mathbf{v}_b, \quad (4)$$

$$G(\mathbf{v}) = \int |\mathbf{v} - \mathbf{v}_b| F(\mathbf{v}_b, t) d\mathbf{v}_b. \quad (5)$$

## 2.1 Conservation

The FPRS collision operator (give in Eq. (3)) preserves mass, momentum and energy which stem from its symmetries<sup>49</sup>. Using the inner product definition  $\langle f, g \rangle_{\mathbf{v}} = \int g(\mathbf{v})f(\mathbf{v})d\mathbf{v}$ , these conservation laws can be expressed as follows:

$$\langle 1, \mathfrak{C}_{ab} \rangle_{\mathbf{v}} = \langle 1, \mathfrak{C}_{ba} \rangle_{\mathbf{v}} \equiv 0 \quad (6)$$

and

$$m_a \langle \mathbf{v}, \mathfrak{C}_{ab} \rangle_{\mathbf{v}} = -m_b \langle \mathbf{v}, \mathfrak{C}_{ba} \rangle_{\mathbf{v}}, \quad (7)$$

$$m_a \left\langle \frac{\mathbf{v}^2}{2}, \mathfrak{C}_{ab} \right\rangle_{\mathbf{v}} = -m_b \left\langle \frac{\mathbf{v}^2}{2}, \mathfrak{C}_{ba} \right\rangle_{\mathbf{v}}. \quad (8)$$

In theory, the FPRS collision operator satisfies the well-known H-theorem. By defining the Boltzmann's entropy of species  $a$ ,  $s_a(t) = -\langle f, \ln f \rangle_{\mathbf{v}}$ , the total entropy of the plasma system can be expressed as  $s_s(t) = \sum_a s_a$ . According to the H-theorem, the total entropy of an isolated plasma system will monotonically increase over time unless there is no change in total entropy, indicating that all  $f_a$  are Maxwellian with a common temperature and average velocity.

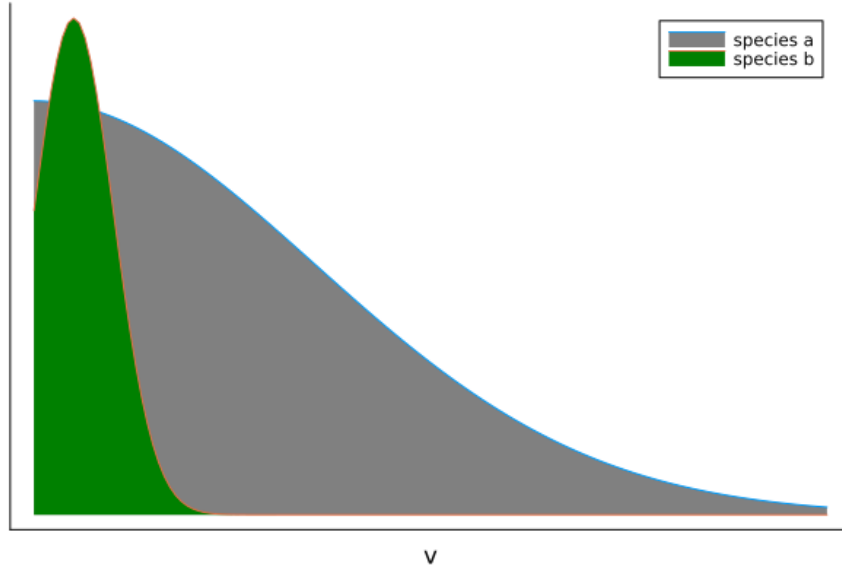


Figure 1: Illustration of the velocity distribution functions in speed coordinate for disparate thermal velocities in a subsonic plasma system.

## 2.2 Normalization

In fusion plasma, the presence of disparate thermal velocities poses additional challenges, arising from the significant mass discrepancy ( $i$ - $e$  collisions) or energy difference ( $D$ - $\alpha$  collisions). This paper specifically focuses on the scenarios where the average velocity is significantly smaller than the thermal velocity. Fig. 1 illustrates the distribution function in speed coordinate when bulk flow of plasma is subsonic with a significant discrepancy in thermal velocities. This discrepancy adds complexity to discretizing the speed, particularly when mapping the background species distribution function to the collision species domain. Previous studies<sup>9,40</sup> have shown that normalizing the distribution function by its local thermal velocity (denoted as  $v_{ath}$  for species  $a$ ) can help to mitigate these challenges. This normalization not only alleviates the need for different meshing requirements between multiple species but also ensures consistent evolution of thermal velocities over time with respect to temperature changes in distribution functions.

We normalize the velocity-space quantities with the local thermal velocity  $v_{ath}$  for species  $a$ , reads:

$$\hat{\mathbf{v}} = \mathbf{v}/v_{ath} . \quad (9)$$

Additionally, the mass, time, charge, thermal velocity, number density  $n_a$ , temperature  $T_a$  and permittivity are normalized by the proton mass  $m_p$ , characteristic time  $\tau_0$ , elementary charge  $e$ , vacuum speed of light  $c_0$ , reference number density  $n_{20} = 10^{-20}\text{m}^{-3}$ , practical unit  $T_k = \text{keV}$  and permittivity of vacuum  $\varepsilon_0$  respectively. The corresponding dimensionless forms of other quantities are determined based on their relationship with these normalized quantities. Thus, we have  $\nabla_{\hat{\mathbf{v}}} = v_{ath}\nabla_{\mathbf{v}}$  and the distribution function can be normalized as follow:

$$\hat{f}(\hat{\mathbf{v}}, t) = n_a^{-1}v_{ath}^3 f(\mathbf{v}, t) . \quad (10)$$

Therefore, the normalized background distribution function and Rosenbluth potentials can be written as:

$$\hat{F}(\hat{\mathbf{v}}_b, t) = n_b^{-1}v_{bth}^3 F(\mathbf{v}_b, t) , \quad (11)$$

$$\hat{H}(\hat{\mathbf{v}}_{ab}) = \frac{v_{bth}}{n_b} H(\mathbf{v}) = \int \frac{1}{\hat{\mathbf{v}}_{ab} - \hat{\mathbf{v}}_b} \hat{F}(\hat{\mathbf{v}}_b, t) d\hat{\mathbf{v}}_b , \quad (12)$$

$$\hat{G}(\hat{\mathbf{v}}_{ab}) = \frac{1}{n_b v_{bth}} G(\mathbf{v}) = \int (\hat{\mathbf{v}}_{ab} - \hat{\mathbf{v}}_b) \hat{F}(\hat{\mathbf{v}}_b, t) d\hat{\mathbf{v}}_b , \quad (13)$$

where  $\hat{\mathbf{v}}_b = \mathbf{v}_b/v_{bth}$  and  $\hat{\mathbf{v}}_{ab} = \mathbf{v}/v_{bth}$ .

Hence, the normalized FPRS collision operator (give in Eq. (2)) of species  $a$  can be expressed as:

$$\hat{\mathcal{C}}(\hat{\mathbf{v}}, t) = n_a^{-1}v_{ath}^3 \mathcal{C} = \sum_{b=1}^{N_s} \frac{n_b}{v_{bth}^3} \hat{\Gamma}_{ab} \hat{\mathcal{C}}_{ab} \quad (14)$$

where

$$\hat{\Gamma}_{ab}(t) = C_{\Gamma} \times 4\pi \left( \frac{Z_a Z_b}{4\pi m_a} \right)^2 \ln \Lambda_{ab} , \quad (15)$$

$$\hat{\mathcal{C}}_{ab}(\hat{\mathbf{v}}, t) = C_{\hat{F}} \hat{F}(\hat{\mathbf{v}}_{ab}, t) \hat{f} + C_{\hat{H}} \nabla_{\hat{\mathbf{v}}_{ab}} \hat{H} \cdot \nabla_{\hat{\mathbf{v}}} \hat{f} + C_{\hat{G}} \nabla_{\hat{\mathbf{v}}_{ab}} \nabla_{\hat{\mathbf{v}}_{ab}} \hat{G} : \nabla_{\hat{\mathbf{v}}} \nabla_{\hat{\mathbf{v}}} \hat{f} . \quad (16)$$

Here,  $\nabla_{\hat{\mathbf{v}}}$  and  $\nabla_{\hat{\mathbf{v}}_{ab}}$  are gradients in normalized velocity space  $\hat{\mathbf{v}}$  and  $\hat{\mathbf{v}}_{ab}$  respectively,  $Z_a$

and  $Z_b$  are the ionization state of species  $a$  and  $b$ , the constant coefficient  $C_\Gamma = \tau_0 \omega_{p0}^4 / (n_{20} c_0^3)$  where  $\omega_{p0} = \sqrt{n_{20} e^2 / (m_p \varepsilon_0)}$ . The coefficients in Eq. (16) are given by:

$$C_{\hat{F}} = 4\pi m_M, \quad C_{\hat{H}} = (1 - m_M) v_{bth} / v_{ath}, \quad C_{\hat{G}} = (v_{bth} / v_{ath})^2 / 2. \quad (17)$$

The normalized like-particle collision operator can be derived from Eq. (16) by replacing  $\hat{F}$  and  $\hat{v}_{ab}$  by  $\hat{f}$  and  $\hat{v}$  respectively, reads:

$$\hat{\mathcal{C}}_{aa}(\hat{v}, t) = 4\pi \hat{f} \hat{f} + \frac{1}{2} \nabla_{\hat{v}} \nabla_{\hat{v}} \hat{G} : \nabla_{\hat{v}} \nabla_{\hat{v}} \hat{f}. \quad (18)$$

After applying Eq. (14), the FPRS collision equation (1) can be rewritten as:

$$\frac{\partial}{\partial t} f(\hat{v}, t) = \frac{n_a}{v_{ath}^3} \hat{\mathcal{C}}. \quad (19)$$

Notes that  $f_l = n_a v_{ath}^{-3} \hat{f}_l$  and the above equation is a semi-normalized equation. It is well-known that normalization involves a non-inertial change of coordinate and consequently, there should be an inertial term stemming from the time derivative in a fully normalized equation<sup>9</sup>. The utilization of  $f_l$  in the time derivative of Eq. (19), instead of  $n_a v_{ath}^{-3} \hat{f}_l$ , can eliminate the non-inertial terms and simplify the complexity of the FPRS collision equation. In order to develop an effective algorithm, we make the assumption that the distribution function,  $f(\hat{v}, t)$ , is a smooth function in the velocity space. It is reasonable that the Coulomb collisions always tends to eliminate the fine structures of the distribution function<sup>11</sup>.

### 3 Discretization of the nonlinear FPRS collision equation

In this study, we adopt a meshfree approach<sup>44</sup> (requiring field nodes) for discretizing the 0D-2V axisymmetric FPRS collision operator. The SHE<sup>12,50</sup> method is employed to discretize the angular components of the normalized FPRS collision operator (as given in Eq. (16)). The King function expansion method presented in Sec. 3.2.1 will be utilized in speed coordinate.

#### 3.1 Angular discretization

We opt for the SHE<sup>12,50</sup> method (utilizing Legendre polynomial expansions<sup>1,23-26,51</sup> when the system is axisymmetric) to analytically adapt the velocity-space discretization in angular dimensions. Unlike previous studies<sup>11,18,52</sup> employing the semi-anisotropic model, we will maintain the full nonlinearity of the FPRS collision operator for all species.

##### 3.1.1 Legendre polynomial expansions

The normalized distribution function of species  $a$  is described by the real function  $\hat{f}(\hat{v}, \theta, t)$  in axisymmetric systems, which can be expanded using Legendre polynomials in normalized velocity space  $\hat{v}(\hat{v}, \theta)$ . It can be expressed as:

$$\hat{f}(\hat{v}, \mu, t) = \sum_{l=0}^{\infty} \hat{f}_l(\hat{v}, t) P_l(\mu). \quad (20)$$

Here,  $\hat{v} = |\mathbf{v}| / v_{ath}$ ,  $\mu = \cos \theta$  and  $0 \leq \theta < \pi$  when choosing the symmetric axis to be the direction  $z$  with base vector  $\mathbf{e}_z$ . The function  $P_l(\mu)$  represents the  $l^{th}$ -order Legendre poly-

nomials. The calculation for the  $l^{\text{th}}$ -order normalized amplitude  $\hat{f}_l(\hat{v}, t)$  can be obtained through the inverse transformation of Eq. (20), expressed as:

$$\hat{f}_l(\hat{v}, t) = \int_{-1}^1 \hat{f}(\hat{v}, \mu, t) P_l(\mu) d\mu. \quad (21)$$

Due to exponential decay of the  $l^{\text{th}}$ -order amplitude at a rate proportion to  $l(l+1)/2$ , as stated in Ref.<sup>11</sup>, there is a natural termination to the expansions. Thus, the function  $\hat{f}(\hat{v}, \mu, t)$  is represented by a finite set of amplitudes  $\hat{f}_l(\hat{v}, t)$ , which are dependent on time  $t$  and magnitude of normalized velocity  $\hat{v} \equiv |\hat{v}|$ . The series in Eq. (20) can be truncated at a maximum order,  $l_M \in \mathbb{N}$ , under the specified condition that  $\max|\hat{f}_l(\hat{v}, t)| \leq \text{Atol}_{df}$ . For species  $b$ , this maximum order will be denoted as  $L_M$ . The convergence of SHE for drift-Maxwellian distribution is depicted in Fig. 2. It shows that  $l_M$  is monotonic function of  $\hat{u}$  when  $\hat{u} \leq 0.5$ . For example with  $\hat{u}_a \leq 2.2 \times 10^{-3}$  and  $\text{Atol}_{df} = 10^{-10}$ , it leads to a maximum order of  $l_M \leq 3$ .

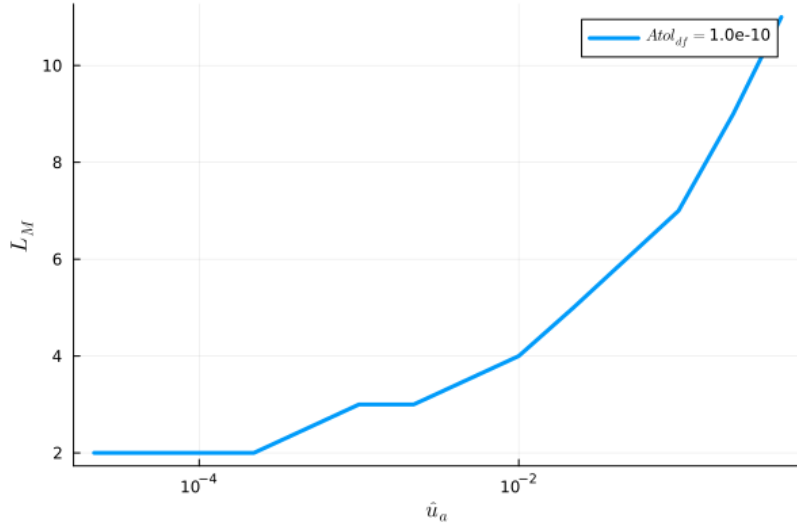


Figure 2: Convergence of SHE for drift-Maxwellian distribution:  $L_M$  as a function of  $\hat{u}_a$  when  $\text{Atol}_{df} = 10^{-10}$ .

Eq. (21) can be computed by utilizing Gaussian quadrature<sup>34</sup> given by:

$$\langle \phi_n([x_i]) | y([x_i]) \rangle_G = \sum_{i=1}^{N_1} w_i \phi_n(x_i) y(x_i), \quad (22)$$

where the subscript  $G$  represents Gaussian,  $[x_i]$  and  $[w_i]$  are the abscissas and weights of Gaussian quadrature with orthogonal basis function  $\phi_n(x)$ ,  $N_1$  represents the number of roots of  $\phi_n(x)$ . Thus, Eq. (21) can be rewritten as:

$$\hat{f}_l(\hat{v}, t) = \sum_{\beta=1}^{l_{M_1}} w_{\mu_\beta} P_l(\mu_\beta) \hat{f}(\hat{v}, \mu_\beta, t) + \mathcal{O}(\text{Atol}_{df}), \quad l = 0, 1, 2, \dots, l_M, \quad (23)$$

where

$$l_{M_1} = l_M + 1. \quad (24)$$

The Gauss-Legendre abscissas will be used as the field nodes for the polar angle direction  $\mu$ . The node  $\mu_\beta$  represents the  $\beta^{\text{th}}$  roots of the Legendre polynomial  $P_l(\mu)$ , out of a total of  $l_{M_1}$  roots. The associated weight  $w_{\mu_\beta}$  can be computed using Fornberg's algorithm<sup>53</sup>.

### 3.1.2 Rosenbluth potentials

In a similar manner, the normalized Rosenbluth potentials of species  $a$ , as described by equations (12)-(13) due to the presence of background species  $b$ , can also be represented in an expanded form, reads:

$$\hat{H}(\hat{v}_{ab}, \mu, t) = 4\pi \sum_{L=0}^{\infty} \hat{H}_L(\hat{v}_{ab}, t) P_L(\mu), \quad (25)$$

$$\hat{G}(\hat{v}_{ab}, \mu, t) = 4\pi \sum_{L=0}^{\infty} \hat{G}_L(\hat{v}_{ab}, t) P_L(\mu). \quad (26)$$

Here,  $\hat{v}_{ab} = |\mathbf{v}|/v_{bth}$ . The  $L^{\text{th}}$ -order amplitudes of  $\hat{H}$  and  $\hat{G}$  can be computed in the following integral form:

$$\hat{H}_L(\hat{v}_{ab}, t) = \frac{1}{2L+1} \frac{1}{\hat{v}_{ab}} (I_{L,L} + J_{L+1,L}), \quad (27)$$

$$\hat{G}_L(\hat{v}_{ab}, t) = \frac{1}{2L+1} \frac{1}{\hat{v}_{ab}} \left( \frac{I_{L+2,L} + J_{L+1,L}}{2L+3} - \frac{I_{L,L} + J_{L-1,L}}{2L-1} \right). \quad (28)$$

The functions  $I_{j,L}$  and  $J_{j,L}$  represent integrals of the normalized background distribution function  $\hat{F}_L(\hat{v}_b, t)$ , following a similar approach as Shkarofsky et. al.<sup>4,13</sup>, reads:

$$I_{j,L}(\hat{v}_{ab}, t) = I_j(\hat{F}_L) = \frac{1}{(\hat{v}_{ab})^j} \int_0^{\hat{v}_{ab}} (\hat{v}_b)^{j+2} \hat{F}_L(\hat{v}_b, t) d\hat{v}_b, \quad (29)$$

$$J_{j,L}(\hat{v}_{ab}, t) = J_j(\hat{F}_L) = (\hat{v}_{ab})^j \int_{\hat{v}_{ab}}^{\infty} \frac{\hat{v}_b^2}{(\hat{v}_b)^j} \hat{F}_L(\hat{v}_b, t) d\hat{v}_b. \quad (30)$$

The normalized distribution function of the background species  $b$ , similar to Eq. (20), can be expressed as:

$$\hat{F}_L(\hat{v}_b, t) = \sum_{\beta=1}^{L_{M_1}} w_{\mu_\beta} P_L(\mu_\beta) \hat{F}(\hat{v}_b, \mu_\beta, t) + \mathcal{O}(Atol_{df}), \quad (31)$$

where  $L_{M_1} = L_M + 1$ .

The partial derivatives of the amplitudes of normalized Rosenbluth potential functions with respect to speed coordinate in axisymmetric velocity space are:

$$\frac{\partial}{\partial \hat{v}_{ab}} \hat{H}_L(\hat{v}_{ab}, t) = \frac{1}{2L+1} \frac{1}{\hat{v}_{ab}^2} [-(L+1)I_{L,L} + (L)J_{L+1,L}], \quad (32)$$

$$\frac{\partial}{\partial \hat{v}_{ab}} \hat{G}_L(\hat{v}_{ab}, t) = \frac{(L-1)I_{L,L} - (L)J_{L-1,L}}{(2L-1)(2L+1)} - \frac{(L+1)I_{L+2,L} - (L+2)J_{L+1,L}}{(2L+1)(2L+3)}. \quad (33)$$



Similarly, the partial derivative of  $\hat{G}_L$  with respect to  $\hat{v}_{ab}$  is:

$$\frac{\partial^2}{\partial \hat{v}_{ab}^2} \hat{G}_L(\hat{v}_{ab}, t) = C_{G L}^{n^2} (I_{L,L} + J_{L-1,L}) + C_{G L}^{p^2} (I_{L+2,L} + J_{L+1,L}) . \quad (34)$$

Here, the coefficients  $C_{G L}^{n^2}$  and  $C_{G L}^{p^2}$  are given by:

$$C_{G L}^{n^2} = -\frac{L(L-1)}{(2L-1)(2L+1)}, \quad (35)$$

$$C_{G L}^{p^2} = \frac{(L+1)(L+2)}{(2L+1)(2L+3)}. \quad (36)$$

### 3.1.3 Weak form of FPRS collision equation

Similar to the expansion of  $\hat{f}(\hat{v})$  (give in Eq. (20)), the normalized FPRS collision operator (14) can also be expanded based on the Legendre polynomials, reads:

$$\hat{\mathcal{C}}(\hat{v}, t) = \sum_{l=0}^{\infty} \hat{\mathcal{C}}_l(\hat{v}, t) P_l(\mu) . \quad (37)$$

The  $l^{th}$ -order amplitude of normalized multi-species nonlinear FPRS operator of species  $a$  is given by:

$$\hat{\mathcal{C}}_l(\hat{v}, t) = \sum_{b=1}^{N_s} \frac{n_b}{v_{bth}^3} \hat{\Gamma}_{ab} \hat{\mathcal{C}}_{lab} . \quad (38)$$

Function  $\hat{\mathcal{C}}_{lab}$  represents the  $l^{th}$ -order amplitude of normalized FPRS collision operator for species  $a$  colliding with species  $b$ , which can be expressed as:

$$\hat{\mathcal{C}}_{lab}(\hat{v}, t) = \sum_{\beta=1}^{l_{M_1}} w_{\mu_\beta} P_l(\mu_\beta) \hat{\mathcal{C}}_{ab}(\hat{v}, \mu_\beta, t) + \mathcal{O}(l_M) . \quad (39)$$

The truncation error term  $\mathcal{O}(l_M)$  is a small quantity dependent on  $l_M$  and will be ignored later. Function  $\hat{\mathcal{C}}_{ab}$  depends on  $\hat{f}_l$  and  $\hat{F}_L$ , as detailed in Appendix B.

Substituting Eq. (20) and Eq. (37) into the FPRS collision equation (19) yields the following equation:

$$\frac{\partial}{\partial t} f_l(\hat{v}, t) = \frac{n_a}{v_{ath}^3} \hat{\mathcal{C}}_l . \quad (40)$$

Multiplying both sides of above equation by  $4\pi m_a v^{j+2} dv$  and integrating over the semi-infinite interval  $v = [0, \infty)$ , simplifying the result gives the  $(j, l)^{th}$ -order FPRS collision equation in weak form:

$$\frac{\partial}{\partial t} \left[ 4\pi \rho_a (v_{ath})^j \int_0^\infty (\hat{v})^{j+2} \hat{f}_l(\hat{v}, t) d\hat{v} \right] = 4\pi \rho_a (v_{ath})^j \int_0^\infty (\hat{v})^{j+2} \hat{\mathcal{C}}_l(\hat{v}, t) d\hat{v}, \quad (41)$$

where the mass density  $\rho_a = m_a n_a$ .

### 3.1.4 Moment constraints

The  $(j, l)^{th}$ -order normalized kinetic moment of species  $a$  is generally defined as:

$$\hat{\mathcal{M}}_{j,l}(t) = \hat{\mathcal{M}}_j(\hat{f}_l) = 4\pi \int_0^\infty (\hat{v})^{j+2} \hat{f}_l(\hat{v}, t) d\hat{v}. \quad (42)$$

The first few orders of  $\hat{\mathcal{M}}_{j,l}$  specifically relative to the conserved moments satisfy the following relations:

$$\hat{n}_a(t) = \hat{\mathcal{M}}_{0,0}, \quad (43)$$

$$\hat{I}_a(t) = \frac{I_a}{\rho_a v_{ath}} = \frac{1}{3} \hat{\mathcal{M}}_{1,1}, \quad (44)$$

$$\hat{K}_a(t) = \frac{K_a}{n_a T_a} = \hat{\mathcal{M}}_{2,0}. \quad (45)$$

Theoretically,  $\hat{n}_a(t)$  is conserved and equal to 1. The momentum is defined as  $I_a(t) = \rho_a \mathbf{u}_a \cdot \mathbf{e}_z$ , the average velocity  $\mathbf{u}_a(t) = n_a^{-1} \int \mathbf{v} f(\mathbf{v}, t) d\mathbf{v}$ , total energy  $K_a(t) = \frac{m_a}{2} \int \mathbf{v}^2 f(\mathbf{v}, t) d\mathbf{v}$  and temperature  $T_a(t) = m_a v_{ath}^2 / 2$ . The normalized average velocity  $\hat{u}_a(t) = \mathbf{u}_a \cdot \mathbf{e}_z / v_{ath}$ , which is equivalent to  $\hat{I}_a$ .

Similar to the normalized kinetic moment (42), we define the  $(j, l)^{th}$ -order normalized kinetic moment of species  $a$  using the following equation:

$$\hat{\mathcal{R}}_{j,l}(t) = \hat{\mathcal{R}}_j(\hat{\mathbf{c}}_l) = 4\pi \int_0^\infty (\hat{v})^{j+2} \hat{\mathbf{c}}_l(\hat{v}, t) d\hat{v}. \quad (46)$$

In particular, the first few orders of  $\hat{\mathcal{R}}_{j,l}$  associated with the conserved qualities can be expressed as:

$$\delta_t \hat{n}_a(t) = \frac{\partial_t n_a}{n_a} = \hat{\mathcal{R}}_{0,0}, \quad (47)$$

$$\delta_t \hat{I}_a(t) = \frac{\partial_t I_a}{\rho_a v_{ath}} = \frac{1}{3} \hat{\mathcal{R}}_{1,1}, \quad (48)$$

$$\delta_t \hat{K}_a(t) = \frac{\partial_t K_a}{n_a T_a} = \frac{3}{2} \hat{\mathcal{R}}_{2,0}. \quad (49)$$

Applying Eqs. (47)-(49), one can derive the following relation:

$$\delta_t \hat{T}_a(t) = \delta_t \hat{K}_a \left[ 2\hat{I}_a \left( \delta_t \hat{I}_a - \hat{I}_a \frac{1}{v_{ath}} \frac{\partial v_{ath}}{\partial t} \right) + \hat{K}_a \frac{1}{v_{ath}} \frac{\partial v_{ath}}{\partial t} \right] \equiv 0. \quad (50)$$

The above equation serves as a convergence criterion for our algorithm in solving the FPRS collision equation (41), which will be referred as identical equation of normalized conserved moments (IENCM).

Mass, momentum and energy conservation (6)-(8) can be reformulated as a function of  $\hat{\mathbf{c}}_{lab}$  (give in Eq. (39)), reads:

$$\left\langle 1, \hat{\mathbf{c}}_{0ab} \right\rangle_{\hat{v}} = \left\langle 1, \hat{\mathbf{c}}_{0ba} \right\rangle_{\hat{v}_b} = 0, \quad (51)$$

$$\rho_a v_{ath} \left\langle \hat{v}, \hat{\mathbf{c}}_{1ab} \right\rangle_{\hat{v}} = -\rho_b v_{bth} \left\langle \hat{v}_b, \hat{\mathbf{c}}_{1ba} \right\rangle_{\hat{v}_b} \quad (52)$$

and

$$\frac{\rho_a (v_{ath})^2}{2} \left\langle (\hat{v})^2, \hat{\mathcal{C}}_{0ab} \right\rangle_{\hat{v}} = -\frac{\rho_b (v_{bth})^2}{2} \left\langle (\hat{v}_b)^2, \hat{\mathcal{C}}_{0ba} \right\rangle_{\hat{v}_b}, \quad (53)$$

where  $\left\langle (\hat{v})^j, g \right\rangle_{\hat{v}}$  denotes the integral of  $4\pi(\hat{v})^{j+2} \cdot g$  with respect to  $\hat{v}$ . These conservation constraints are activated when enforcing discrete conservation (details provided in Sec. 4.2) of the normalized FPRS collision operator (give in Eq. (16)). Otherwise, they serve as indicators to evaluate the performance of our algorithm.

### 3.2 Speed coordinate

Assuming that the function  $f(v, \mu)$  is smooth in the velocity space, all the amplitudes  $\hat{f}_l(\hat{v})$  are continuously differentiable. it is also assumed that the system evolves continuously over times. In contrast to the previous work using the multi-quadric radial basis function<sup>31</sup>, a new function named King (details in Appendix A) will be employed in speed coordinate to develop an effective algorithm.

#### 3.2.1 King method

The new King function, which is associated with the first class of modified Bessel functions, can be defined as following:

$$\mathcal{K}_l(v; \iota, \sigma) = \frac{(l + 1/2)}{\sigma^2 \sqrt{2|\iota|} v} \left( \frac{|\iota|}{\iota} \right)^l e^{-\sigma^{-2}(v^2 + \iota^2)} \text{Besseli} \left( \frac{2l + 1}{2}, 2 \frac{|\iota|}{\sigma^2} v \right). \quad (54)$$

In this context, the independent variable  $v \in [0, \mathbb{R}^+]$  and the parameter  $l \in \mathbb{N}$ , representing the order of the King function. The parameters  $\iota$  and  $\sigma$  are characteristic parameters of the King function, satisfying  $\sigma \in \mathbb{R}^+$  and  $\iota \in \mathbb{R}$ .

If two known groups of characteristic parameters  $(\iota_1, \sigma_1)$  and  $(\iota_2, \sigma_2)$ , each with respective weights  $\hat{n}_{a_1}$  and  $\hat{n}_{a_2}$ , satisfy

$$\left| \frac{\sigma_1}{\sigma_2} - 1 \right| + \left| \frac{\iota_1}{\iota_2} - 1 \right| \leq rtol, \quad (55)$$

we claim that the King function  $\mathcal{K}_l(v; \iota_1, \sigma_1)$  and  $\mathcal{K}_l(v; \iota_2, \sigma_2)$  are identical with parameters  $(\iota_0, \sigma_0)$ . Here,  $rtol$  is a given relative tolerance with a default value,  $rtol = 10^{-10}$ . The weight of  $\mathcal{K}_l(v; \iota_0, \sigma_0)$  is given by  $\hat{n}_{a_0} = \hat{n}_{a_1} + \hat{n}_{a_2}$ . Eq. (55) serves as the indistinguishable condition of the King function.

The  $l^{\text{th}}$ -order King function,  $\mathcal{K}_l(\hat{v}; \hat{u}_a, \hat{v}_{ath})$  (give in Eq. (54)) has the same asymptotic behaviour (details in Appendix A) as the  $l^{\text{th}}$ -order amplitude of the normalized distribution function,  $\hat{f}_l(\hat{v}, t)$  (give in Eq. (23)). Therefore, we can effectively approximate  $\hat{f}_l(\hat{v}, t)$  using the King function as follows:

$$\hat{f}_l(\hat{v}, t) = C_3 \sum_{s=1}^{N_K} [\hat{n}_{a_s} \mathcal{K}_l(\hat{v}; \hat{u}_{a_s}, \hat{v}_{ath_s})]. \quad (56)$$

This equation represents the King function expansion (KFE) under the finitely distinguishable independent features hypothesis introduced in reference<sup>54</sup>. In this context, the constant coefficient  $C_3 = \sqrt{2\pi}/\pi^{3/2}$ . The number of basis function,  $N_K \in \mathbb{N}^+$  is a pre-

determined value at the initial step but will be determined by the L01jd2NK scheme later (Sec. in 3.2.2). The convergence of KFE can be established by utilizing Wiener's Tauberian theorem<sup>55</sup>, as demonstrated in Ref.<sup>54</sup>. Similarly, for the  $l^{\text{th}}$ -order amplitude of the normalized distribution function of the background species  $b$ ,  $\hat{F}_L(\hat{v}_b, t)$  can be approximated as:

$$\hat{F}_L(\hat{v}_b, t) = C_3 \sum_{r=1}^{N_K} [\hat{n}_{b_r} \mathcal{K}_L(\hat{v}; \hat{u}_{b_r}, \hat{v}_{b_{th_r}})] . \quad (57)$$

The King method (Eq. (56)) is a moment convergence algorithm demonstrated in Sec. 5.1. In this study, we assume that the characteristic parameters  $\hat{n}_{a_s}$ ,  $\hat{u}_{a_s}$  and  $\hat{v}_{ath_s}$  are independent of  $l$ . This assumption allows us to approximate the normalized function  $\hat{f}(\hat{v}, \mu, t)$  by  $N_K$  Gaussian functions as follows,  $\hat{f}(\hat{v}, \mu, t) = \sum_{s=1}^{N_K} \frac{1}{\pi^{3/2}} \frac{\hat{n}_{a_s}}{\hat{v}_{ath_s}^3} e^{-(\hat{v} - \hat{u}_{a_s} \mathbf{e}_z)^2}$ . This approximation is reasonable and efficient, particularly when each sub-component  $\mathcal{K}_l$  is not far from a thermal equilibrium state ( $|\hat{u}_{a_s}| \ll 1$ ).

Multiplying both sides of Eq. (56) by  $4\pi\hat{v}^{j+2}d\hat{v}$  and integrating over the semi-infinite interval  $\hat{v} = [0, \infty)$  yields the following characteristic parameter equations (CPEs):

$$\hat{\mathcal{M}}_{j,l}(t) = \begin{cases} C_{M_j}^l \sum_{s=1}^{N_K} \hat{n}_{a_s} (\hat{v}_{ath_s})^j \left[ 1 + \sum_{k=1}^{j/2} C_{j,l}^k \left( \frac{\hat{u}_{a_s}}{\hat{v}_{ath_s}} \right)^{2k} \right], & l \in 2\mathbb{N}, \\ C_{M_j}^l \sum_{s=1}^{N_K} \hat{n}_{a_s} (\hat{v}_{ath_s})^j \left( \frac{\hat{u}_{a_s}}{\hat{v}_{ath_s}} \right)^l \left[ 1 + \sum_{k=1}^{(j-1)/2} C_{j,l}^k \left( \frac{\hat{u}_{a_s}}{\hat{v}_{ath_s}} \right)^{2k} \right], & l \in 2\mathbb{N} + 1. \end{cases} \quad (58)$$

The coefficients  $C_{j,l}^k$  and  $C_{M_j}^l$  are given by:

$$C_{j,l}^k = 2^k \frac{(2l+1)!! C_{(j-l)/2}^k}{(2l+2k+1)!!}, \quad (59)$$

$$C_{M_j}^l = \frac{1}{2^{(j-l)/2}} \frac{(l+j+1)!!}{(2l-1)!!}. \quad (60)$$

In particular, when all  $\hat{u}_{a_s}$  are zero, the CPEs will be:

$$\hat{\mathcal{M}}_{j,l}(t) = C_{M_j}^l \sum_{s=1}^{N_K} \hat{n}_{a_s} (\hat{v}_{ath_s})^j, \quad l \in 2\mathbb{N}. \quad (61)$$

Note that  $\hat{\mathcal{M}}_{j,l}$  represents the exact value of normalized kinetic moment (42) computed from the amplitude of distribution function before being smoothed by King method. The parameters  $\hat{n}_{a_s}$ ,  $\hat{u}_{a_s}$  and  $\hat{v}_{ath_s}$  can be determined by solving any  $3N_K$  different orders  $(j, l)$  characteristic parameter constraint equations (58). In order to solve these characteristic parameter equations, the following section provides three specific algorithms, L01jd2nh, L01jd2 and L01jd2NK which are convergent for higher-order moments.

### 3.2.2 L01jd2NK scheme for parameters $\hat{n}_{a_s}$ , $\hat{u}_{a_s}$ and $\hat{v}_{ath_s}$

Generally, any  $3N_K$  normalized kinetic moments,  $\hat{\mathcal{M}}_{j,l}$ , can be utilized in the CPEs (58) to determine parameters  $\hat{n}_{a_s}$ ,  $\hat{u}_{a_s}$  and  $\hat{v}_{ath_s}$ . Due to the rapid damping of the higher-order

harmonics, the first few harmonics in the expression (20) contain much of the most important physics for many plasma physical problems of interest. Therefore, assuming that parameters  $\hat{n}_{a_s}$ ,  $\hat{u}_{a_s}$  and  $\hat{v}_{ath_s}$  are independent of  $l$ , we propose the following scheme by selecting the kinetic moments of the first two amplitudes of normalized distribution function with orders,

$$(j, l) \in \{(2j_p + l, l) | j_p \in \mathbb{N}, 0 \leq l \leq 1, 0 \leq 2j_p + l < 3N_K\} . \quad (62)$$

This will be referred as the L01jd2nh scheme. In particular, when  $(j, l) = (1, 1)$ , CPEs represented by Eq. (58) yields:

$$\sum_{s=1}^{N_K} \hat{n}_{a_s} \hat{u}_{a_s} = \hat{\mathcal{M}}_{1,1}/3 = \hat{u}_a . \quad (63)$$

When  $(j, l) = (0, 0)$  and  $(j, l) = (2, 0)$ , CPEs gives:

$$\sum_{s=1}^{N_K} \hat{n}_{a_s} = \hat{\mathcal{M}}_{0,0} = \hat{n}_a, \quad (64)$$

$$\sum_{s=1}^{N_K} \hat{n}_{a_s} \left( \frac{3}{2} \hat{v}_{ath_s}^2 + \hat{u}_{a_s}^2 \right) = \hat{\mathcal{M}}_{2,0} = \frac{3}{2} + (\hat{u}_a)^2 . \quad (65)$$

The Eqs. (63)-(65) serve as conservation constraints and will be utilized as the constraint equations for L01jd2nh, as well as the subsequent L01jd2 scheme, during the optimization process. This indicates that when  $N_K \geq 1$ , the L01jd2nh scheme can ensure convergence of mass, momentum and energy during the optimization process.

After computing the normalized kinetic moments  $\hat{\mathcal{M}}_{j,l}$ , employing Romberg integral given by Eq. (73), the parameters  $\hat{n}_{a_s}$ ,  $\hat{u}_{a_s}$  and  $\hat{v}_{ath_s}$  can be solved from CPEs (58) by utilizing a least squares method<sup>56</sup> (LSM), specifically Levenberg-Marquardt<sup>57,58</sup> method. In order to enclose the nonlinear FPRS collision equation (41), the approximation of  $\hat{f}_l$  when  $l \geq 2$  can be achieved through the utilization of King function expansion (56) with established characteristic parameters. Subsequently, analytical expressions for the first two derivatives of  $\hat{f}_l(\hat{v}, t)$  with respect to  $\hat{v}$  can be derived based on Eq. (56). The number of King function at the  $(k + 1)^{th}$  time step will be given by:

$$N_K(t_{k+1}) = N_K(t_k) - dN_K(t_k), \quad (66)$$

$$dN_K(t_k) = \begin{cases} 0, & \text{Eq. (55) == false,} \\ 1, & \text{Eq. (55) == true.} \end{cases} \quad (67)$$

When the parameters  $\hat{n}_{a_s}$  of species  $a$  are all nearly constant, a more effective scheme named L01jd2, rather than L01jd2nh, can be utilized. Here, assuming that  $\hat{n}_{a_s}$  are constants and any  $2N_K$  normalized kinetic moments,  $\hat{\mathcal{M}}_{j,l}$  could be employed in CPEs (58) to determine the parameters  $\hat{u}_{a_s}$  and  $\hat{v}_{ath_s}$ . In the L01jd2 scheme,  $N_k$  will remain constant and

$$(j, l) \in \{(2j_p - l, l) | j_p \in \mathbb{N}^+, 0 \leq l \leq 1, 1 \leq j_p < N_K\} . \quad (68)$$

The L01jd2NK scheme is obtained by integrating the L01jd2nh scheme and the L01jd2 scheme, using the criterion given by

$$\delta \hat{n}_{a_s} = |\hat{n}_{a_s}(t_{k+1}) - \hat{n}_{a_s}(t_k)| / \hat{n}_{a_s}(t_k) . \quad (69)$$

When the parameters  $\hat{n}_{a_s}$  of species  $a$  satisfy  $\delta \hat{n}_{a_s} \leq rtol_{nhC}$ ,  $s = 1, 2, \dots, N_K$ , where

$rtol_{nhC}$  is a specified relative tolerance, the L01jd2 scheme will be executed. Otherwise, the L01jd2nh scheme will be performed within L01jd2NK scheme. In this paper, unless otherwise stated, the parameter  $rtol_{nhC} = 0.1$ .

Especially, when all parameters  $\hat{u}_{a_s}$  are zero, the L01jd2nh scheme simplifies to:

$$(j, l) \in \{(2j_p - 2, l) | j_p \in \mathbb{N}^+, 1 \leq j_p \leq 2N_K, l = 0\}, \quad (70)$$

and the L01jd2 scheme becomes:

$$(j, l) \in \{(2j_p, l) | j_p \in \mathbb{N}^+, 1 \leq j_p \leq N_K, l = 0\}. \quad (71)$$

In theory, when all  $\hat{u}_{a_s}$  are zero, enforcing Eqs. (63)-(65) yields:

$$\hat{\mathcal{M}}_{1,1} = 0, \quad \hat{\mathcal{M}}_{0,0} = \frac{2}{3}\hat{\mathcal{M}}_{2,0} = 1. \quad (72)$$

Eq. (70) and Eq. (71) show that if  $N_K$  increases by one, the convergence order  $j$  increases by two in the L01jd2 scheme and by four in the L01jd2nh scheme when  $N_K \geq 2$ .

It is worth to note that the L01jd2NK can be extended to be a self-adaptive scheme called Ld1jd2NK, in order to address the general situation where characteristic parameters in KFE (56) are dependent on  $l$ . This improved scheme will utilize a comprehensive set of normalized kinetic moments,  $\hat{\mathcal{M}}_{j,l}$ , incorporate self-adaptive field nodes and will be further developed in future studies.

### 3.2.3 Discretization of speed coordinate

In order to calculate the normalized kinetic moments  $\hat{\mathcal{M}}_{j,l}$  (42) in CPEs (58) and the Shkarofsky's integrals (give in Eqs. (29)-(30)), a set of field nodes in speed coordinate is required. Applying uniform field nodes  $[v_\alpha]$  with a total number of  $N_n = 2^{n_2} + 1$ , within a normalized speed domain of  $[0, \hat{v}_M]$ . The spacing,  $\Delta \hat{v}_\alpha$ , is then determined as  $\Delta \hat{v}_\alpha = \hat{v}_M / 2^{n_2}$  where  $n_2 \in \mathbb{N}^+$ . The default value for parameters  $\hat{v}_M$  and  $n_2$  are set at  $\hat{v}_M = 10$  and  $n_2 = 7$ , unless otherwise stated. Therefore, the default number of nodes,  $N_n$  will be 129.

The normalized kinetic moments  $\hat{\mathcal{M}}_{j,l}$  (42) will be calculated using the Romberg integral<sup>46</sup> method. For convenience, the value and its relative error can be expressed as:

$$\hat{\mathcal{M}}_{j,l}(t), Error \left( \hat{\mathcal{M}}_{j,l} \right) = \left\langle ([\hat{v}_\alpha])^j | \hat{f}_l([\hat{v}_\alpha], t) \right\rangle_R. \quad (73)$$

Here,  $\left\langle (\hat{v})^j | \hat{f}_l(\hat{v}) \right\rangle_R$  denotes the Romberg integral of function  $(\hat{v})^{j+2} \hat{f}_l(\hat{v})$ , and  $Error \left( \hat{\mathcal{M}}_{j,l} \right)$  represents the estimated upper bound of the integral error of  $\hat{\mathcal{M}}_{j,l}$ . The set  $[\hat{v}_\alpha]$  represents the uniform nodes (depicted as red points in Fig. 3). Similarly, the computation of Eq. (46) will also be performed using Romberg integral:

$$\hat{\mathcal{R}}_{j,l}(t), Error \left( \hat{\mathcal{R}}_{j,l} \right) = \left\langle ([\hat{v}_\alpha])^j | \hat{\mathcal{C}}_l([\hat{v}_\alpha], t) \right\rangle_R. \quad (74)$$

The relative errors,  $Error \left( \hat{\mathcal{M}}_{j,l} \right)$  and  $Error \left( \hat{\mathcal{R}}_{j,l} \right)$  can serve as indicators to evaluate the quality of field nodes. These indicators could be utilized in constructing a self-adaptive algorithm which will be developed in the future.

The Shkarofsky's integrals, given in Eqs. (29)-(30), involve variable upper/lower bound integration and can be computed on a set of refined grids, as shown in Fig. 3. To create

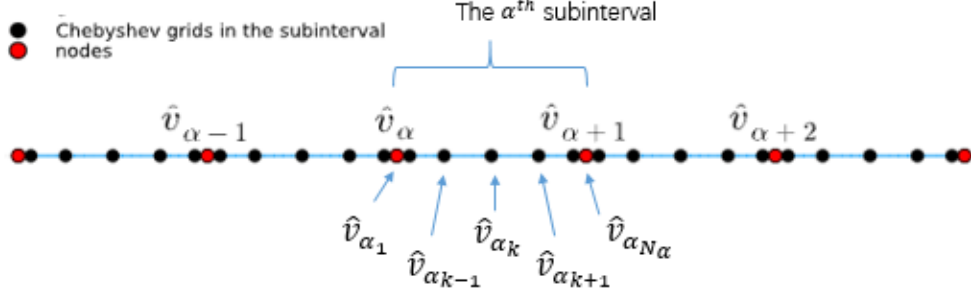


Figure 3: Discretization of speed coordinate: field nodes and the Chebyshev grids in the subinterval.

the  $\alpha^{\text{th}}$  subinterval  $[\hat{v}_{\alpha k}], k = 1, 2, \dots, N_\alpha$ , we add  $N_\alpha - 2$  auxiliary grids in the inner interval  $[\hat{v}_\alpha, \hat{v}_{\alpha+1}]$ , as showed in Fig. 3. For background species  $b$ , let  $z_{\alpha k} = v_{abth}\hat{v}_{\alpha k}$  where  $z = \hat{v}_{ab}$  and  $v_{abth} = v_{ath}/v_{bth}$ . The Shkarofsky's integrals can be calculated using parallel Clenshaw-Curtis (CC) quadrature, which is a type of Gauss-Chebyshev quadrature<sup>34</sup>. This method can be expressed as:

$$I_{j,L}(z_\alpha, t) = \begin{cases} 0, & \alpha = 1, \\ \frac{1}{(z_\alpha)^j} \sum_{s=2}^{\alpha} \langle ([z_{s_k}]^j | \hat{F}_L([z_{s_k}], t) \rangle_{CC}, & 2 \leq \alpha \leq 2^{n_2} + 1, \end{cases} \quad (75)$$

$$J_{j,L}(z_\alpha, t) = \begin{cases} 0, & \alpha = 2^{n_2} + 1, \\ (z_\alpha)^j \sum_{s=\alpha}^{2^{n_2}} \langle ([z_{s_k}]^{-j} | \hat{F}_L([z_{s_k}], t) \rangle_{CC}, & 1 \leq \alpha \leq 2^{n_2}. \end{cases} \quad (76)$$

Here, the Clenshaw-Curtis quadrature can be expressed as:

$$\langle ([x_k]^j | g([x_k]) \rangle_{CC} = \sum_{k=1}^{N_\alpha} w_k (x_k)^{j+2} g(x_k). \quad (77)$$

The set  $[x_k]$  is the Gauss collection on the quadrature domain where  $k = 1, 2, \dots, N_\alpha$ . The corresponding integral weight  $w_k$  is calculated according to Fornberg's algorithm<sup>53</sup>. Function  $\hat{F}_L(\hat{v}_{ab}, t)$  denotes the normalized background distribution function of species  $a$ . This function can be easily obtained by mapping the analytic function,  $\hat{F}_L(\hat{v}_b, t)$  given by Eq. (57), onto the normalized speed  $\hat{v}_{ab}$ . This process of mapping can be expressed as:

$$\hat{F}_L(\hat{v}_{ab}, t) = \hat{F}_L(v_{abth}\hat{v}_b, t). \quad (78)$$

In this paper, the number of auxiliary Chebyshev grids in subintervals,  $N_\alpha$ , is fixed at a given constant  $N_0$  and the auxiliary grids (depicted as black points in Fig. 3) are only utilized in the step for calculating the Shkarofsky's integrals. Consequently, the total number of field nodes in speed coordinate is determined by  $N_v = (N_0 - 1)(N_n - 2) + N_0$  and  $N_{v2} = l_{M_1} \times N_v$  for the total velocity space. Given the default value of  $N_0 = 7$  unless otherwise specified, we obtain  $N_v = 769$ . It should be noted that  $N_v$  and  $N_{v2}$  are primarily utilized in the Rosenbluth potentials step (Sec. 3.1.2), while the maximum number of field nodes in the velocity space is determined by number of nodes,  $N_n$ . Additionally, it is worth mentioning that the King function serves as a smoothing step, combined with the implicit time discretization given in Sec. 4, enabling our algorithm to surpass the classical CFL condition limit.

#### 4 Implicit temporal discretization and nonlinear conservation constraints

The weak form of FPRS collision equation (41) in discrete form can be expressed as:

$$\frac{\partial}{\partial t} \left[ 4\pi\rho_a(v_{ath})^j \left\langle ([\hat{v}_\alpha])^j | \hat{f}_l([\hat{v}_\alpha], t) \right\rangle_R \right] = 4\pi\rho_a(v_{ath})^j \left\langle ([\hat{v}_\alpha])^j | \hat{\mathcal{C}}_l([\hat{v}_\alpha], t) \right\rangle_R, \quad (79)$$

where  $0 \leq l \leq l_M$  and  $j$  satisfies Eq. (68). When integrals (73)-(74) are convergent and accurate, the above equation represents the  $(j, l)^{th}$ -order kinetic moment evolution equation, reads:

$$\frac{\partial}{\partial t} \left[ \rho_a(v_{ath})^j \hat{\mathcal{M}}_{j,l} \right] = \rho_a(v_{ath})^j \hat{\mathcal{R}}_{j,l}. \quad (80)$$

The initial equations for the conserved moments are given by Eqs. (47)-(49). Thermal velocity,  $v_{ath}$  is a function of  $\rho_a$ ,  $I_a$  and  $K_a$ , reads:

$$v_{ath} = \sqrt{\frac{2}{3} \left( \frac{2K_a}{\rho_a} - \left( \frac{I_a}{\rho_a} \right)^2 \right)}. \quad (81)$$

The final semi-discrete scheme for the nonlinear FPRS collision equations is obtained by incorporating the aforementioned equations, including the weak form of collision equation (79), the FPRS collision operators (38)-(39), (134), King function expansion (56) and the characteristic parameter equations (58), with convergence criterion (50) and conservation constraint equations (51)-(53). From now on, the subscript and superscript "k" will represent the time level.

##### 4.1 Implicit temporal discretization

A standard trapezoidal<sup>45</sup> scheme, which is a second-order implicit Range-Kutta method, can be formulated as follows:

$$A^{k+1} = A^k + \frac{1}{2} \Delta t_k \left( \frac{\partial}{\partial t} A^k + \frac{\partial}{\partial t} A^{k+1*} \right), \quad (82)$$

where  $\Delta t_k = t_{k+1} - t_k$  represents the current time-step size. During the inner iteration to optimize the convergence of  $A$  at  $(k+1)^{th}$  time level,  $A^{k+1}$  denotes the value of  $A$  in the  $i^{th}$  stage at  $(k+1)^{th}$  timestep, while  $A^{k+1*}$  represents the value of  $A$  at the  $(i-1)^{th}$  stage during  $(k+1)^{th}$  time level, where  $i = 1, 2, \dots, N_{in}$ . The maximum number of the inner iteration during each time level is denoted as  $N_{in}$  and is typically set to a default value of 10.

By employing the trapezoidal scheme for time integration, the  $l^{th}$ -order weak form of FPRS collision equation (79) at a given node  $\alpha$  and time level  $k+1$  is discretized as follows:

$$c_{k+1} \rho_a^{k+1} (v_{ath}^{k+1})^j \left\langle ([\hat{v}_\alpha^{k+1}])^j | \hat{f}_l([\hat{v}_\alpha^{k+1}], t_{k+1}) \right\rangle_R = c_k \rho_a^k (v_{ath}^k)^j \left\langle ([\hat{v}_\alpha^k])^j | \hat{f}_l([\hat{v}_\alpha^k], t_k) \right\rangle_R + \Delta t_k \left[ \rho_a^k (v_{ath}^k)^j \left\langle ([\hat{v}_\alpha^k])^j | \hat{\mathcal{C}}_l([\hat{v}_\alpha^k], t_k) \right\rangle_R + \rho_a^{k+1} (v_{ath}^{k+1})^j \left\langle ([\hat{v}_\alpha^{k+1}])^j | \hat{\mathcal{C}}_l([\hat{v}_\alpha^{k+1}], t_k) \right\rangle_R \right]. \quad (83)$$

The coefficients  $c_k$  and  $c_{k+1}$  represent the temporal weights for Range-Kutta method, while for the trapezoidal scheme, they both equal 2. Upon discretization, implicit methods for the Fokker-Planck equation lead to a complex system of nonlinear algebraic equa-



tions, necessitating an effective nonlinear solver strategy for its solution.

In this study, we rely on the King method for this task. Under the assumption that the characteristic parameters are independent of  $l$ , which can be disregarded in future analysis, the  $l^{\text{th}}$ -order amplitude of distribution function of species  $a$  at the  $\alpha^{\text{th}}$  node and  $(k+1)^{\text{th}}$  time level is given by:

$$\hat{f}_l(\hat{v}_\alpha^{k+1}, t_{k+1}) = C_3 \sum_{s=1}^{N_K} [\hat{n}_{a_s}^{k+1} \mathcal{K}_l(\hat{v}_\alpha^{k+1}; \hat{u}_{a_s}^{k+1}, \hat{v}_{ath_s}^{k+1})] . \quad (84)$$

The characteristic parameters can be obtained by solving the CPEs (58), at  $(k+1)^{\text{th}}$  time level, as given by:

$$\hat{\mathcal{M}}_{j,l}(t_{k+1}) = \begin{cases} C_{Mj}^l \sum_{s=1}^{N_K} \hat{n}_{a_s}^{k+1} (\hat{v}_{ath_s}^{k+1})^j \left[ 1 + \sum_{i=1}^{j/2} C_{j,l}^i \left( \frac{\hat{u}_{a_s}^{k+1}}{\hat{v}_{ath_s}^{k+1}} \right)^{2i} \right], & l = 0, \\ C_{Mj}^l \sum_{s=1}^{N_K} \hat{n}_{a_s}^{k+1} (\hat{v}_{ath_s}^{k+1})^j \left( \frac{\hat{u}_{a_s}^{k+1}}{\hat{v}_{ath_s}^{k+1}} \right)^l \left[ 1 + \sum_{i=1}^{(j-1)/2} C_{j,l}^i \left( \frac{\hat{u}_{a_s}^{k+1}}{\hat{v}_{ath_s}^{k+1}} \right)^{2i} \right], & l = 1. \end{cases} \quad (85)$$

Here, the normalized kinetic moment at the  $(k+1)^{\text{th}}$  time level is calculated using Romberg scheme (73) as follows:

$$\hat{\mathcal{M}}_{j,l}(t_{k+1}), Error \left( \hat{\mathcal{M}}_{j,l}(t_{k+1}) \right) = \left\langle ([\hat{v}_\alpha^{k+1}])^j | \hat{f}_l([\hat{v}_\alpha^{k+1}], t_{k+1}) \right\rangle_R . \quad (86)$$

By applying  $\hat{f}_l(\hat{v}_\alpha, t_{k+1})$ , the  $l^{\text{th}}$ -order amplitude of FPRS collision operator in Eq. (83) can be formulated as:

$$\hat{\mathcal{C}}_l(\hat{v}^{k+1}, t_{k+1}) = \sum_{b=1}^{N_s} \frac{n_b^{k+1}}{(v_{bth}^{k+1})^3} \hat{\Gamma}_{ab}^{k+1} \sum_{\beta=1}^{l_{M1}} w_{\mu_\beta} P_l(\mu_\beta) \hat{\mathcal{C}}_{ab}(\hat{\mathbf{v}}^{k+1}, \mu_\beta, t) . \quad (87)$$

The normalized kinetic FPRS collision operator,  $\hat{\mathcal{C}}_{ab}$ , satisfies Eq. (134), which can be expressed as:

$$\hat{\mathcal{C}}_{ab}(\hat{\mathbf{v}}^{k+1}, t_{k+1}) = \hat{\mathcal{C}}_{ab} \left[ \hat{f}_0(\hat{v}_\alpha^{k+1}, t_{k+1}), \dots, \hat{f}_l(\hat{v}_\alpha^{k+1}, t_{k+1}), \dots, \hat{f}_{l_M}(\hat{v}_\alpha^{k+1}, t_{k+1}), \right. \\ \left. \hat{F}_0(v_{abth}^{k+1} \hat{v}_\alpha^{k+1}, t_{k+1}), \dots, \hat{F}_L(v_{abth}^{k+1} \hat{v}_\alpha^{k+1}, t_{k+1}), \dots, \hat{F}_{l_M}(v_{abth}^{k+1} \hat{v}_\alpha^{k+1}, t_{k+1}) \right] . \quad (88)$$

In order to properly address those nonlinear algebraic equations represented by Eqs. (83)-(88), it is imperative to impose constraints for ensuring conservation properties. By employing the Romberg integration with appropriate field nodes, we are able to achieve high-precision values for moments, including number density, momentum and energy. Building upon these high-precision values, according to manifold theory, we rely on backward error analysis to guarantee exact conservation.

#### 4.2 Conservation enforcing

The accuracy of integrals (47)-(49) can be guaranteed for at least one during two-species collision processes (details in Sec. 5.1). The convergence criterion for conservation

with high accuracy in two-species collision processes at the  $(k + 1)^{th}$  time level can be expressed as:

$$\min(\delta_t \hat{C}_a^{k+1}, \delta_t \hat{C}_b^{k+1}) \ll 1, \quad (89)$$

where

$$\delta_t \hat{C}_a^{k+1} = |Error(\delta_t \hat{n}_a^{k+1})| + |Error(\delta_t \hat{I}_a^{k+1})| + |Error(\delta_t \hat{K}_a^{k+1})| \quad (90)$$

and similar for  $\delta_t \hat{C}_b^{k+1}$ . The aforementioned criterion will also be employed to evaluate the quality of field nodes as described in Sec. 3.2.3.

From manifold theory<sup>41</sup>, post-step projection to manifolds maintains a consistent convergence rate, and conservation properties can be preserved as long as the local solution errors remain sufficiently small. Consequently, incorporating a conservation strategy into our algorithm becomes feasible. This strategy enforces discrete conservation equations (51)-(53), by utilizing the more precise integrals, such as those for species  $b$  described by Eqs. (47)-(49), to provide more accurate representations during two-species collision processes. The convergence of this conservation strategy will occur when the criterion given by Eq. (89) is satisfied.

According to the conservation constraint represented by Eqs. (52)-(53), by applying relation (47)-(49), the rates of momentum and energy change of species  $a$  with respect to time at the  $(k + 1)^{th}$  time level can be theoretically expressed as:

$$\frac{\partial}{\partial t} I_a^{k+1} = -\frac{\partial}{\partial t} I_b^{k+1}, \quad (91)$$

$$\frac{\partial}{\partial t} K_a^{k+1} = -\frac{\partial}{\partial t} K_b^{k+1}. \quad (92)$$

When enforcing conservation (47), all rates of change in number density will be zero, yields:

$$n_a^{k+1} = n_a^k. \quad (93)$$

However, it is not feasible to achieve an exact numerical realization of Eqs. (91)-(92) using a general integral scheme. When all the local errors, represented by  $Error(\delta_t \hat{I}^{k+1})$  and  $Error(\delta_t \hat{K}^{k+1})$  are sufficiently small through the utilization of appropriate field nodes, we can enforce Eqs. (91)-(92) by selecting the more precision one between species  $a$  and species  $b$ . For example, if the local errors of species  $b$  are small means  $\delta_t \hat{C}_a^{k+1} \geq \delta_t \hat{C}_b^{k+1}$ , then according to manifold theory, let

$$\frac{\partial}{\partial t} I_a^{k+1} := -\frac{\partial}{\partial t} I_b^{k+1}, \quad (94)$$

$$\frac{\partial}{\partial t} K_a^{k+1} := -\frac{\partial}{\partial t} K_b^{k+1} \quad (95)$$

in each stage at the  $(k + 1)^{th}$  time level.

In the trapezoidal method, the values of momentum and energy at the  $(k + 1)^{th}$  time level are calculated through an inner iteration at the  $(k + 1)^{th}$  time level, for species  $a$ , can

be expressed in the following form:

$$I_a^{k+1} = I_a^k + \frac{1}{2} \Delta t_k \left( \frac{\partial}{\partial t} I_a^k + \frac{\partial}{\partial t} I_a^{k+1*} \right), \quad (96)$$

$$K_a^{k+1} = K_a^k + \frac{1}{2} \Delta t_k \left( \frac{\partial}{\partial t} K_a^k + \frac{\partial}{\partial t} K_a^{k+1*} \right). \quad (97)$$

The inner iteration at each time level will be terminated when the thermal velocity of all plasma species in the  $i^{th}$  stage at  $(k+1)^{th}$  time level satisfies the following condition, for species  $a$  reads:

$$\left| \frac{v_{ath}(t_{k+1_i})}{v_{ath}(t_{k+1_{i-1}})} - 1 \right| \leq 10^{-6}, \quad i \geq 2, \quad (98)$$

Consequently, the average velocity and thermal velocity of species  $a$  at the  $(k+1)^{th}$  timestep can be expressed as:

$$u_a^{k+1} = \frac{I_a^{k+1}}{\rho_a^{k+1}}, \quad (99)$$

$$v_{ath}^{k+1} = \sqrt{\frac{2}{3} \left[ \frac{2K_a^{k+1}}{\rho_a^{k+1}} - (u_a^{k+1})^2 \right]}. \quad (100)$$

Thus, the normalized average velocity of species  $a$  is calculated as  $\hat{u}_a^{k+1} = u_a^{k+1}/v_{ath}^{k+1}$ . By applying Eqs. (63)-(65), we obtain:

$$\hat{\mathcal{M}}_{0,0}(t_{k+1}) \equiv 1, \quad (101)$$

$$\hat{\mathcal{M}}_{1,1}(t_{k+1}) = 3\hat{u}_a^{k+1}, \quad (102)$$

$$\hat{\mathcal{M}}_{2,0}(t_{k+1}) = 3/2 + (\hat{u}_a^{k+1})^2. \quad (103)$$

The conservation enforcing algorithm will be presented in the following Algorithm 1.

---

**Algorithm 1** Algorithm for enforcing conservation during two-species collision processes in each stage at the  $(k+1)^{th}$  time level.

---

From inputs  $\hat{\mathcal{R}}_{j,l}(t_{k+1})$  and *Error*  $(\hat{\mathcal{R}}_{j,l}(t_{k+1}))$  of species  $a$  and species  $b$ :

Initial  $\frac{\partial}{\partial t} n^{k+1}, \frac{\partial}{\partial t} I^{k+1}, \frac{\partial}{\partial t} K^{k+1}$  for species  $a$  and species  $b$  according to Eqs. (47)-(49)

1 Evaluate whether  $\min(\delta_t \hat{C}_a^{k+1}, \delta_t \hat{C}_b^{k+1}) \ll 1$  (give in Eq. (89))

**If**  $\delta_t \hat{C}_a^{k+1} \geq \delta_t \hat{C}_b^{k+1}$

$$2A \quad \frac{\partial}{\partial t} I_a^{k+1} = -\frac{\partial}{\partial t} I_b^{k+1}, \quad \frac{\partial}{\partial t} K_a^{k+1} = -\frac{\partial}{\partial t} K_b^{k+1}$$

**Else**

$$2B \quad \frac{\partial}{\partial t} I_b^{k+1} = -\frac{\partial}{\partial t} I_a^{k+1}, \quad \frac{\partial}{\partial t} K_b^{k+1} = -\frac{\partial}{\partial t} K_a^{k+1}$$

**End**

3 Let  $\frac{\partial}{\partial t} n^{k+1} = 0$  for all species

4 Output  $\frac{\partial}{\partial t} n^{k+1}, \frac{\partial}{\partial t} I^{k+1}, \frac{\partial}{\partial t} K^{k+1}$  for all species.

---

By implementing the conservation enforcing scheme mentioned above, the accuracy of the conservation (51)-(53) will be determined by the precision of the more accurate

species rather than the less precise species. It is worth noting that small local solution errors of  $\delta_t \hat{n}$  (47),  $\delta_t \hat{I}$  (48) and  $\delta_t \hat{K}$  (49) for at least one species during two-species Coulomb collision process, represented by Eq. (89), are a necessary condition for convergence. This condition will be verified at each stage and every timestep in our algorithm. The main procedure for enforcing conservation during two-species collision processes is outlined in the following pseudo-code (Algorithm 2).

---

**Algorithm 2** Algorithm for FPRS collision equation with conservation constrains

---

From inputs initial distribution function for all species,  $f(\mathbf{v}, t_0)$ :

Initial  $n_a^0, u_a^0, v_{ath}^0$  and  $\hat{f}_l(\hat{v}, t_0)$  (23) with parameter  $l_{M_1}$  for all species

Initial  $\hat{M}_{0,0}(t_0), \hat{M}_{1,1}(t_0)$  and  $\hat{M}_{2,0}(t_0)$  according to Eq. (86) for all species

**While** Time termination condition == **False**

**For**  $i = 1, 2, \dots, N_{in}$

**For**  $a = 1, 2, \dots, N_s$

1 Compute the normalized kinetic moments  $\hat{M}_{j,l}(t_{k+1})$  (86), except for  $\hat{M}_{0,0}(t_{k+1}), \hat{M}_{1,1}(t_{k+1})$  and  $\hat{M}_{2,0}(t_{k+1})$

2 Solve CPEs (85) to obtain the parameters  $\hat{n}_{a_s}^{k+1}, \hat{u}_{a_s}^{k+1}, \hat{v}_{ath_s}^{k+1}$  and update  $\hat{f}_l(\hat{v}, t_{k+1})$  (84)

**For**  $b = 1, 2, \dots, N_s$

3a Evaluate  $\frac{\partial}{\partial \hat{v}} \hat{f}_l(\hat{v}_\alpha^{k+1}, t_{k+1}), \frac{\partial^2}{\partial \hat{v}^2} \hat{f}_l(\hat{v}_\alpha^{k+1}, t_{k+1})$  according to KFE (84)

3b Evaluate  $\hat{F}_L(v_{abth}^{k+1}, t_{k+1})$  according to the process of mapping (78)

4 Calculate Shkarofsky's integrals (29)-(30) employing CC quadrature (75)-(76)

5 Compute the amplitudes of Rosenbluth potentials and its related derivatives according to Eqs. (27)-(28) and Eqs. (32)-(34)

6 Update the normalized FPRS collision operator,  $\hat{\mathcal{C}}_{ab}$  according to Eq. (88)

7 Update the amplitudes of FPRS collision operator,  $\hat{\mathcal{C}}_{lab}$  according to Eq. (87)

8 Evaluate  $\hat{\mathcal{R}}_{j,l}(t_{k+1})$  and  $Error(\hat{\mathcal{R}}_{j,l}(t_{k+1}))$  by calculating the Romberg integral (74)

**If** Conservation enforcing == **True**

9A Update  $\frac{\partial}{\partial t} n_a^{k+1}, \frac{\partial}{\partial t} I_a^{k+1}, \frac{\partial}{\partial t} K_a^{k+1}$  according to conservation enforcing algorithm 1

**Else**

9B Update  $\frac{\partial}{\partial t} n_a^{k+1}, \frac{\partial}{\partial t} I_a^{k+1}, \frac{\partial}{\partial t} K_a^{k+1}$  according to Eqs. (47)-(49)

**End**

**End** (for species  $b$ )

**End** (for species  $a$ )

10 Condition for inner iteration represented by Eq. (98) == **False** || **Break**

**End** (for inner iteration)

11 Compute  $n_a^{k+1}, I_a^{k+1}, K_a^{k+1}$  and  $\hat{f}_l(v_\alpha^{k+1}, t_{k+1})$  according to Eqs. (47)-(49) and (83)

12 Update  $u_a^{k+1}$  (99),  $v_{ath}^{k+1}$  (100),  $\hat{M}_{0,0}(t_{k+1})$  (101),  $\hat{M}_{1,1}(t_{k+1})$  (102) and  $\hat{M}_{2,0}(t_{k+1})$  (103)

13 Update parameters  $l_{M_1}$  (24),  $N_K$  (66) at the new time level

**End** (for time level)

---

(Notes: The symbols "==" and "||" respectively denote the logical operator "equal to" and "or".)

### 4.3 Timestep

The Coulomb collision process encompasses multiple dynamical times-scales (such as inter-species time-scale, self-collision time-scale, relaxation time-scale of conserved moments, et. al.), making it stiff. In this paper, a timestep of  $\Delta t = 2^{-5}$  (unless otherwise stated) will be utilized for fixed timestep cases. Self-adaptive timestep will be employed (unless otherwise stated) to improve the algorithm performances, which is determined by the following algorithm:

$$\Delta_{t_{k+1}} = \min \left( ratio_{dt_k} \times \Delta_{t_k}, ratio_{M_j} \times \left| \frac{1}{y^k} \frac{\partial y^k}{\partial t} \right| \right). \quad (104)$$

Here, the subscripts  $k$  denotes the time level and  $y$  represents momentum  $I$  and total energy  $K$  for all species.  $\Delta_{t_k} = 1$  at the initial timestep. Parameters  $ratio_{dt_k}$  and  $ratio_{M_j}$  are given constants, with default values of  $ratio_{dt_k} = 1.1$  and  $ratio_{M_j} = 0.01$  in this paper. For cases utilizing self-adaptive timestep, nearly all timesteps satisfy  $10^{-3} \leq \Delta t \leq 0.1$ .

As a contrast, the explicit timestep size determined by the CFL condition<sup>2</sup> is calculated as follows:

$$\Delta_{t_0}^{Exp} = R_{CFL} \times \min_{\substack{l=0,1,\dots,l_M \\ a,b=1,2,\dots,N_s}} \left\{ \frac{\Delta \hat{v}}{A_{lab}}, \frac{(\Delta \hat{v})^2}{D_{lab}} \right\}. \quad (105)$$

In this equation, the parameter  $R_{CFL} = 0.1$  is utilized in explicit method to ensure long-term stability. Additionally,  $A_{lab}$  and  $D_{lab}$  represent the transport coefficients in the FPRS collision operator (give in Eq. (3)), reads:

$$A_{lab} = \frac{n_a}{v_{ath}^3} \frac{n_b}{v_{bth}^3} \times C_{\hat{H}} \hat{\Gamma}_{ab} \frac{\partial}{\partial \hat{v}_{ab}} \hat{H}_L, \quad (106)$$

$$D_{lab} = \frac{n_a}{v_{ath}^3} \frac{n_b}{v_{bth}^3} \times C_{\hat{G}} \hat{\Gamma}_{ab} \frac{\partial^2}{\partial \hat{v}_{ab}^2} \hat{G}_L. \quad (107)$$

This explicit timestep size (105) will not be directly utilized in our algorithm, but rather serve as a reference for our timestep represented by Eq. (104).

## 5 Numerical results

In order to demonstrate the convergence and effectiveness of our method for solving the Fokker-Planck collision equation (19), we will assess the performance of our algorithm with various examples of different degrees of complexity.

In the benchmarks conducted in this session, the initial distribution functions for particles at  $t = 0$  are drifting Maxwellian distributions with a specified number density  $n_a$ , average velocity  $u_a$  and temperature  $T_a$ , which can be written as:

$$f(\mathbf{v}, t) = \frac{n_a}{v_{ath}^3} \hat{f}(\hat{v}, \mu, t) = \frac{1}{\pi^{3/2}} \frac{n_a}{(v_{ath})^3} \sum_{s=1}^{N_{K_0}} \left[ \frac{\hat{n}_{a_s}}{(\hat{v}_{ath_s})^3} e^{-(\hat{v} - \hat{u}_{a_s} \mathbf{e}_z)^2} \right], \quad (108)$$

For all cases, all the parameters are normalized values with units defined in Sec.2.2. Unless otherwise specified, the default values for  $(n_2, N_0)$  are set to  $(7, 7)$  as specified in section. 3.2.3 and the number of King functions  $N_{K_0}$  is set to 1 at the initial timestep. Hence, the default values of parameters are  $\hat{n}_{a_s} = \hat{v}_{ath_s} = 1$  and  $\hat{u}_{a_s} = \hat{u}_a$ . For L01jd2 scheme, the number of King function  $N_K$  during time evolution will remain equivalent to  $N_{K_0}$ ,

while a maximum value of  $N_K$  will be specified in L01jd2NK and L01jd2nh schemes. In this paper, the default solver is L01jd2NK scheme when  $\max(m_M, 1/m_M) \sim 1$ , and L01jd2 scheme when  $\max(m_M, 1/m_M) \gg 1$ .

### 5.1 Two-species thermal equilibration

In this instance, we demonstrate the convergence performance of our algorithm on two-species thermal equilibration, a widely used benchmark for evaluating schemes to solve the Fokker-Planck collision equation. The parameters for this case are  $m_a = 2$ ,  $m_b = 3$ ,  $Z_a = Z_b = 1$ ,  $n_a = n_b = 1$ ,  $u_a = u_b = 0$ ,  $T_a = 10$  and  $T_b = 20$ . Theoretically values for the temperature and momentum at equilibrium state can be obtained using conservation equations for momentum and energy:

$$I_s^k = \sum_a (m_a n_a^k u_a^k) \equiv \sum_a (m_a n_a^0 u_a^0), \quad (109)$$

$$K_s^k = \frac{1}{2} \sum_a [3n_a^k T_a^k + m_a n_a^k (u_a^k)^2] \equiv \frac{1}{2} \sum_a [3n_a T_a^0 + m_a n_a^0 (u_a^0)^2]. \quad (110)$$

The initial total momentum and energy are  $I_s^0 = 0$  and  $K_s^0 = 45$  respectively. According to the conservation equations (109)-(110), the final average velocity and temperatures of the thermal equilibrium state should be  $u_\infty = 0$  and  $T_\infty = 15$  respectively.

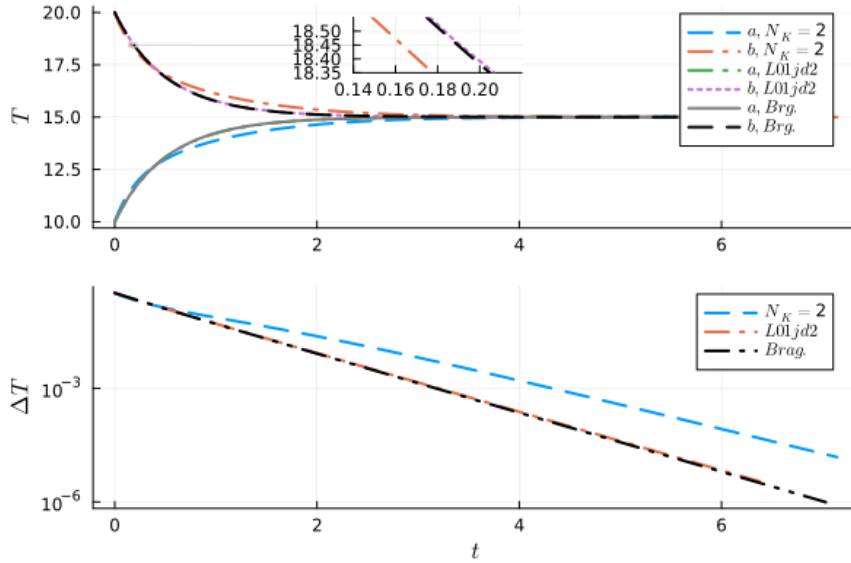


Figure 4: Two-species temperature equilibration with fixed timestep,  $\Delta t = 2^{-5}$ : Temperatures (upper) and their relative disparity of temperatures (lower),  $\Delta T = |T_a^k - T_b^k| / (T_a^k + T_b^k)$  as functions of time. The color lines represent the numerical solution while the gray and black lines represent the Braginskii's values.

The two-species thermal equilibration model, as described by Braginskii<sup>59</sup>, is presented through a semianalytical asymptotic temperature evolution equation:

$$\frac{\partial}{\partial t} T_a = \nu_T^{ab} (T_a - T_b), \quad (111)$$

where the characteristic collision rate  $\nu_T^{ab}$  is given by<sup>48</sup> :

$$\nu_T^{ab} \approx 441.72 \times \frac{\sqrt{m_a m_b} (Z_a Z_b)^2 n_b}{(m_a T_b + m_b T_a)^{3/2}} \ln \Lambda_{ab} . \quad (112)$$

The temperature relaxation time is defined as  $\tau_T^{ab} = 1/\nu_T^{ab}$ . The characteristic time  $\tau_0$  will be equivalent to the initial temperature relaxation time unless otherwise specified.

The semianalytical equation (111) is solved employing the standard explicit Runge-Kutta<sup>45</sup> method of order 4, and the results are depicted in Fig. 4. The temperatures are plotted as functions of time and compared against the numerical solution of our kinetic model with a fixed timestep of  $\Delta t = 2^{-5}$  and L01jd2NK scheme with the maximum number of King function  $N_K = 2$ . Fig. 4 demonstrates excellent agreement between our fully kinetic model and the semianalytical solution. Furthermore, upon comparing the results of L01jd2 ( $N_K \equiv 1$  in this case) and L01jd2NK ( $N_K = 2$ ) with the semianalytical solution, it is observed that the temperature decay rate of L01jd2NK is a slightly faster than that of Braginskii's within the initial time interval ( $t < 0.58$  in this case), but this trend reverses when  $t \geq 0.58$  (Similar to the behavior observed in the FVM's approach as shown in the Fig.14 of Ref.<sup>2</sup>). However, the results of L01jd2 scheme strictly adhere to the semianalytical solution, as shown in the lower subplot of Fig. 4.

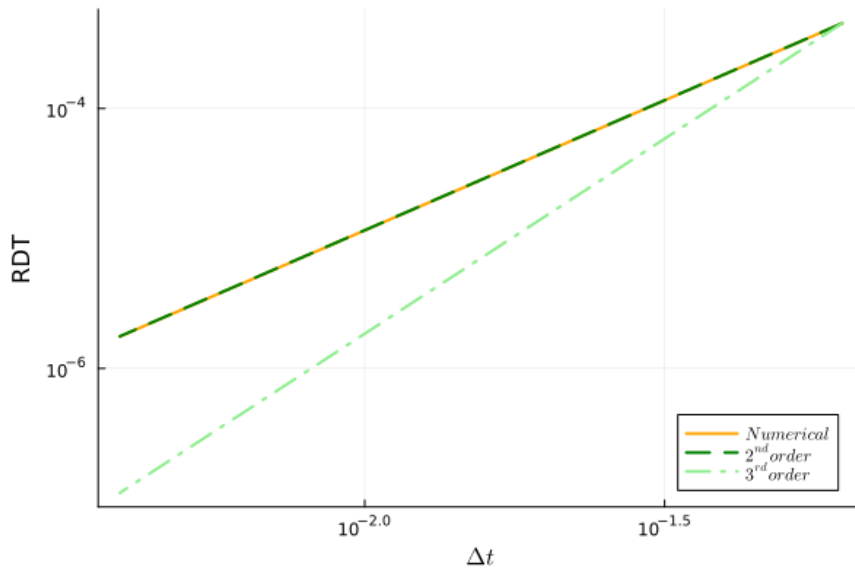


Figure 5: Two-species temperature equilibration with fixed timestep,  $\Delta t$ : Demonstration of second-order convergence of the time discretization scheme.

The solid line in Fig. 5 depicts the relative deviation of temperature between our kinetic model and reference values  $T_{ref}$ , given by  $RDT = |T_{kin} - T_{ref}|/T_{ref}$  at  $t = 0.5$ , as a function of the fixed timestep,  $\Delta t$ . The reference value,  $T_{ref}$ , is computed using a sufficiently small timestep,  $\Delta t = 2^{-11}$ , in our kinetic model. The results indicate that our algorithm exhibits  $2^{nd}$ -order convergence in time discretization.

The temporal evolution of errors in the conserved quantities, specifically discrete num-

ber (or mass) density, momentum, energy conservation,

$$\Delta n_s(t_k) = (N_s)^{-1} \sum_a |n_a^k/n_a^0 - 1|, \quad (113)$$

$$\Delta I_s(t_k) = |I_s^k/I_s^0 - 1|, \quad (114)$$

$$\Delta K_s(t_k) = |K_s^k/K_s^0 - 1|, \quad (115)$$

and entropy conservation,

$$\Delta s_s(t_k) = (s_s^k - s_s^{k-1}) / [\Delta t (s_s^k + \delta s_s)], \quad (116)$$

are depicted in Fig. 6 for varying number of field nodes with  $(n_2, N_0)$ . Here, the parameter  $\delta s_s$  is given by  $\delta s_s = \delta_\zeta^{-1}(|s_s^0| + |s_s^{end}|)$ , where  $\zeta = |s_s^0 s_s^{end}| / (s_s^0 s_s^{end})$  and  $s_s^{end}$  are the value of  $s_s$  at the end time level.  $\delta s_s \equiv 0$  in all cases except for the last one in Sec. 5. Since entropy conservation serves as a convergence criterion for our algorithm, a first-order implicit scheme is utilized to calculate the entropy change, as defined by Eq. (116).

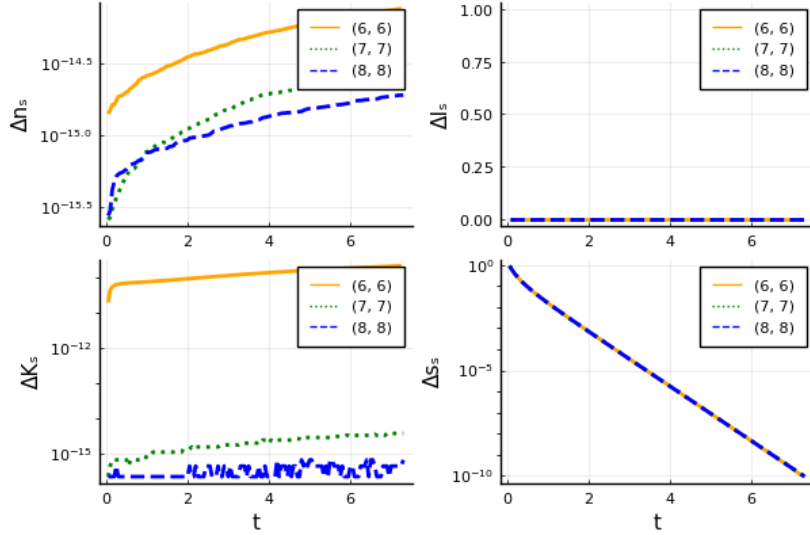


Figure 6: Two-species temperature equilibration without enforcing conservation: Discrete conservation errors as functions of time and number of field nodes,  $(n_2, N_0)$ .

The discrete mass conservation is achieved with high precision for all given  $(n_2, N_0)$ , even without enforcing conservation. The discrete momentum conservation and H-theorem are preserved all the time. The discrete error of the energy conservation rapidly decreases with an increase of number of field nodes and reaches the level of round-off error when  $(n_2, N_0) = (8, 8)$ , corresponding to a total number of nodes  $N_n = 257$ . Since  $l_{M_1} = 1$  for two-species temperature equilibration, the total number of field nodes is  $N_{v_2} = l_{M_1} \times N_v = 1793$  for Rosenbluth potentials step 3.1.2. The results of  $\Delta K_s$  in Fig. 6 indicate that the convergence order of the velocity-space discretization scheme is about 16. The convergence order<sup>60</sup> of a discrete algorithm is evaluated using:

$$order = [1/\log(2)] \log(\epsilon_{n_2-1}/\epsilon_{n_2}). \quad (117)$$

Here, we assume that  $\epsilon_{n_2} = \mathcal{O}[(h_{n_2})^{order}]$ , where  $h_{n_2}$  represents the grid size with grid number is  $2^{n_2}$ . The number of time steps in this case is determined to be  $N_t = 122$ , based



on the termination condition  $\Delta s_s \leq 10^{-10}$ .

The relative errors of Romberg integrals for the first few orders of  $\hat{\mathcal{R}}_{j,l}$  (46),  $\delta_t \hat{n}_a$  (47),  $\delta_t \hat{I}_a$  (48),  $\delta_t \hat{K}_a$  (49) and convergence criterion  $\delta_t \hat{T}_a$  (50) during two-species Coulomb collisions are depicted in Fig. 7 and Fig. 8 when  $(n_2, N_0) = (7, 7)$ . It is evident that all the relative errors are at the level of round-off error. The maximal errors occur at the initial moment and diminish to the level of round-off error over a collision time scale. The fact that convergence criterion  $\delta_t \hat{T}_a$  consistently equals the theoretical value indicates that our algorithm exhibits strong convergence properties.

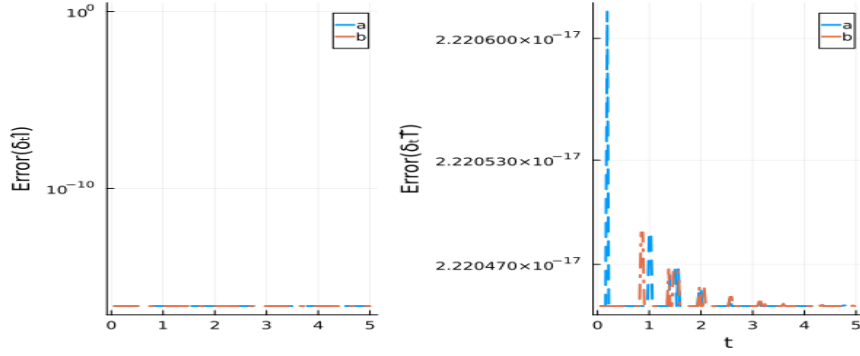


Figure 7: Two-species temperature equilibration without enforcing conservation: Romberg integral errors of  $\delta_t \hat{I}$  and convergence criterion  $\delta_t \hat{T}$  respect to time  $t$  when  $(n_2, N_0) = (7, 7)$ .

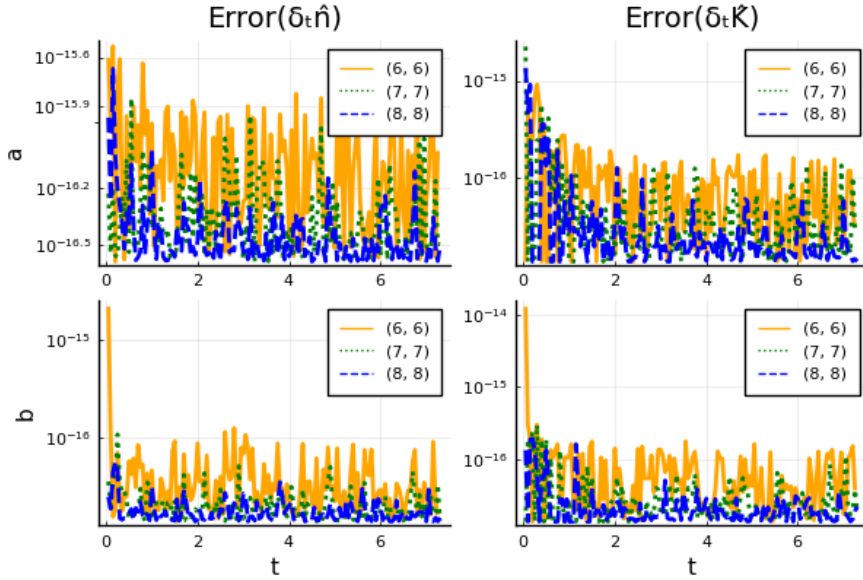


Figure 8: Two-species temperature equilibration without enforcing conservation: Romberg integral errors of  $\delta_t \hat{n}$  and  $\delta_t \hat{K}$  respect to time for collision species  $a$  and  $b$  with various  $(n_2, N_0)$ .

The relationship between relative errors and orders  $(n_2, N_0)$  is depicted in Fig. 8. In all cases, the relative errors are significantly smaller than one, indicating that condition (give in Eq. (89)) is consistently satisfied. Specifically, the relative errors of species  $a$  remain at the level of round-off error throughout. However, the orange solid line representing

species  $b$  in Fig. 8 reveals that both the relative errors of  $\delta_t \hat{n}_b$  and  $\delta_t \hat{K}_b$  are two orders of magnitude larger than the round-off error when  $(n_2, N_0) = (6, 6)$  at initial moments. This discrepancy can result in discrete errors in energy conservation (see Fig. 6). Furthermore, Fig. 8 also indicates that as the number of grids  $(n_2, N_0)$  increases, the errors of species  $b$  rapidly decrease to the level of round-off error. This suggests that integrals (47)-(49) will be accurate at least for one species during two-species collision process and the integration accuracy for any less accurate species can be improved by refining field nodes.

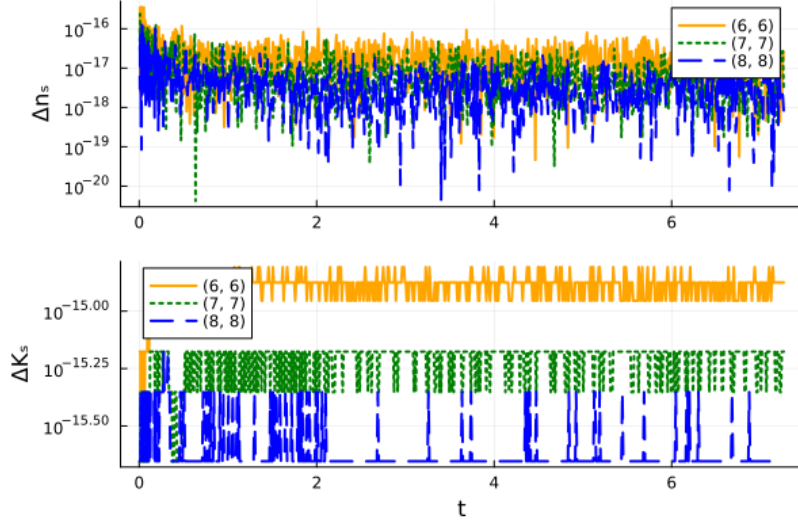


Figure 9: Two-species temperature equilibration with enforcing conservation: Discrete conservation errors as functions of time and number of field nodes,  $(n_2, N_0)$ .

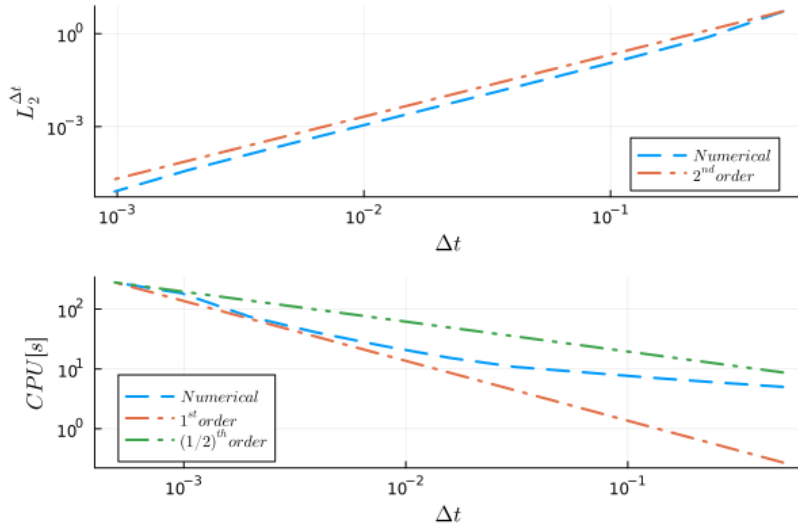


Figure 10: Two-species temperature equilibration with fixed timestep,  $\Delta t$ : Demonstration of  $2^{th}$ -order convergence of time discretization scheme in  $L_2$ -norm and the CPU time as function of timestep,  $\Delta t$ .

When implementing the conservation enforcing algorithm 1, the time histories of the associated conservation errors,  $\Delta n_s$  and  $\Delta K_s$  are plotted in Fig. 9 for varying number of

field nodes,  $(n_2, N_0)$ . As anticipated, precise discrete conservation can be achieved for all given  $(n_2, N_0)$ .

We can also demonstrate second-order time convergence of the trapezoidal scheme by computing the  $L_2$ -norm of relative difference in solution compared to a reference solution,

$$L_2^{\Delta t} = \sqrt{\langle f_l^{\Delta t} / f_l^{\Delta t_{ref}} - 1, f_l^{\Delta t} / f_l^{\Delta t_{ref}} - 1 \rangle}. \quad (118)$$

Here,  $f_l^{\Delta t_{ref}}$  is the solution obtained using a reference timestep size,  $\Delta t_{ref} = 2^{-11}$ ; refer to Fig. 10 (upper) when  $(n_2, N_0) = (7, 7)$ . As expected, second-order convergence is realized with the refinement of  $\Delta t$ . The CPU time as a function of  $\Delta t$  when  $(n_2, N_0) = (7, 7)$  is also plotted in the lower subplot of Fig. 10. The total solution time scales approximately as  $\mathcal{O}(1/\Delta t)$ . This first-order correlation arises from the rapid convergence of inner iteration, typically requiring only a few iterations even with different timesteps, as demonstrated by Fig. 23 in Sec. 5.4. Compared to the explicit timestep,  $\Delta t^{Exp} \approx 1.5 \times 10^{-3}$  in this case estimated by Eq. (105), a timestep greater than two order of magnitude can be used in our algorithm with acceptable precision.

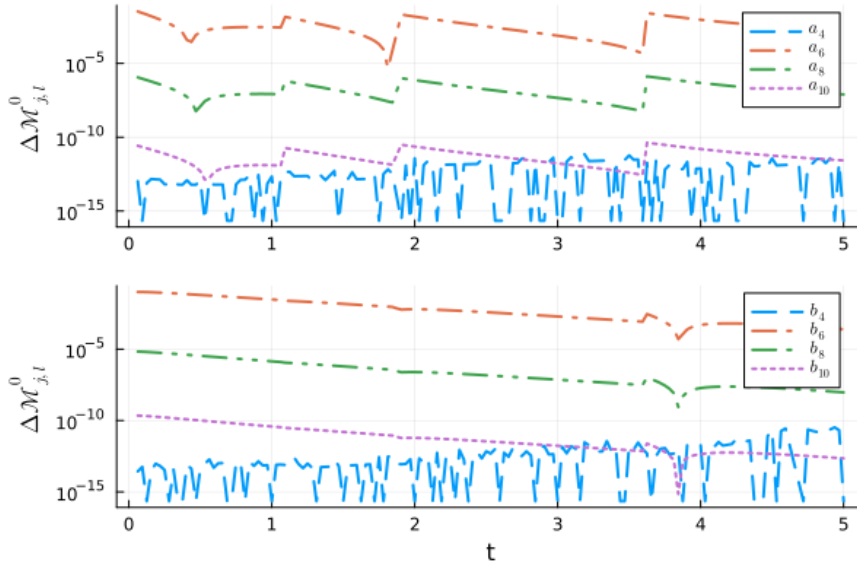


Figure 11: Two-species temperature equilibration without enforcing conservation: Time discretization errors of the non-conserved moments as functions of time with various  $j$  when  $\Delta t = 2^{-5}$ ,  $N_K = 2$  and  $(n_2, N_0) = (7, 7)$ .

Fig. 11 illustrates the time discretization errors of the non-conserved moments,  $\Delta \hat{\mathcal{M}}_{j,l}$  as functions of time with various  $j$  when  $j \geq 4$ . Here,  $\Delta t = 2^{-5}$ ,  $N_K = 2$  and  $(n_2, N_0) = (7, 7)$ . The quantity  $\Delta \hat{\mathcal{M}}_{j,l}$  is defined as:

$$\Delta \hat{\mathcal{M}}_{j,l} = \left| \hat{\mathcal{M}}_{j,l}(t_{k+1}) - \hat{\mathcal{M}}_{j,l}(t_{k+1}) \right| / \left| \hat{\mathcal{M}}_{j,l}(t_{k+1}) - \hat{\mathcal{M}}_{j,l}(t_k) \right| \quad (119)$$

which measures the relative error resulting from velocity discretization during optimization process. The symbols  $\hat{\mathcal{M}}_{j,l}$  and  $\hat{M}_{j,l}$  represent the normalized kinetic moment (42), which are computed from the amplitude of distribution function before and after being smoothed by King method, respectively. By applying Eqs. (63)-(65) in L01jd2NK scheme,

the time discretization errors of the conserved moments (give in Eq. (119)) for all species will be exactly zero. Furthermore, convergence of the optimization of  $(j, l)^{th}$ -order normalized kinetic moments is achieved when  $\Delta \hat{\mathcal{M}}_{j,l} \leq rtol_{NK}$ , where  $rtol_{NK}$  is a given relative tolerance. In this study, we set parameter  $rtol_{NK}$  to  $10^{-11}$  unless otherwise specified. As shown in Fig. 11, the moment with order  $j = 6$  exhibits a maximum deviation not exceeding 6.6% for all species under consideration when  $N_K = 2$ . Additionally, the time discretization errors for the convergent order,  $j = 4$ , are generally no greater than  $10^{-11}$ .

The high-order moment convergence property of the present method is further investigated. Fig. 12 illustrates the time discretization errors of the non-conserved moments,  $\Delta \hat{\mathcal{M}}_{j,l}$ , at  $t_k \approx 0.47$  as functions of  $N_K$  with various  $j$ . For this test, a refined timestep and field nodes,  $\Delta t = 2^{-6}$  and  $(n_2, N_0) = (8, 8)$  will be utilized. As depicted in Fig. 12, all the discretization errors of the non-conserved moments,  $\Delta \hat{\mathcal{M}}_{j,l}$ , decrease as  $N_K$  increase. Furthermore, it is observed that the highest convergent order is  $j = 2$  when  $N_K = 1$ ,  $j = 4$  when  $N_K = 2$  and  $j = 6$  when  $N_K = 3$ . Therefore, it can be concluded that King method (Sec. 3.2.1) is a moment convergence algorithm.

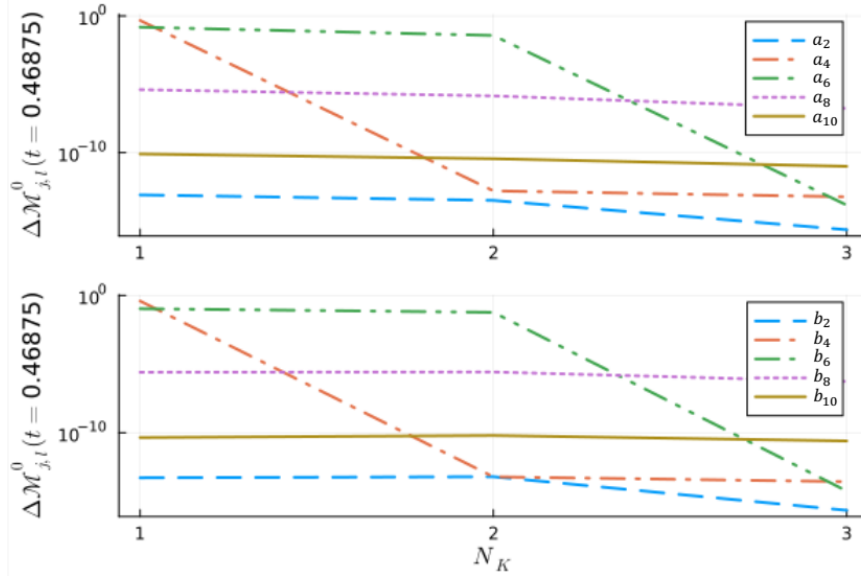


Figure 12: Two-species temperature equilibration without enforcing conservation: Time discretization errors of the non-conserved moments as functions of  $N_K$  with various  $j$  when  $\Delta t = 2^{-6}$ ,  $t_k \approx 0.47$  and  $(n_2, N_0) = (8, 8)$ .

In situations with large thermal velocity disparity where  $v_{th_f}/v_{th_s} \gg 1$ , the maximum value of normalized speed  $\hat{v}_M$  at  $(k+1)^{th}$  time level will be determined by a more sophisticated method, for species  $a$ , can be described as follow:

$$\delta_l^0 (\hat{v}_M^{k+1})^j \hat{f}_l(\hat{v}_M^{k+1}, t_k) + \delta_l^1 (\hat{v}_M^{k+1})^{j+1} \left| \hat{f}_l(\hat{v}_M^{k+1}, t_k) \right| = 4.44 \times 10^{-17}, \quad j = 2.5N_K. \quad (120)$$

Applying information at the  $k^{th}$  time level and solving the above equation, the optimized value of  $\hat{v}_M$  at  $(k+1)^{th}$  time level can be obtained. It is evident that  $\hat{v}_M$  will vary across different time levels, while remaining constant within a single time level. This step ensures that the value of distribution function at the right boundary of speed can be effectively

disregarded as zero.

For example, when  $T_a = 10$  and  $T_b = 500$ , with all other parameters remaining the same as in the previous case, the temperatures calculated by the L01jd2NK scheme using a fixed timestep of  $\Delta t = 2^{-5}$ ,  $N_K = 2$  and  $(n_2, N_0) = (8, 7)$  are depicted as functions of time in Fig. 13. As anticipated, the results show good agreement between our fully kinetic model and the semianalytical solution. By comparing Fig. 14 and Fig. 6, we can see that achieving the same level of precision with an increased temperature difference requires more refined field nodes by increasing  $n_2$ , without using self-adaptive  $(n_0, N_2)$ .

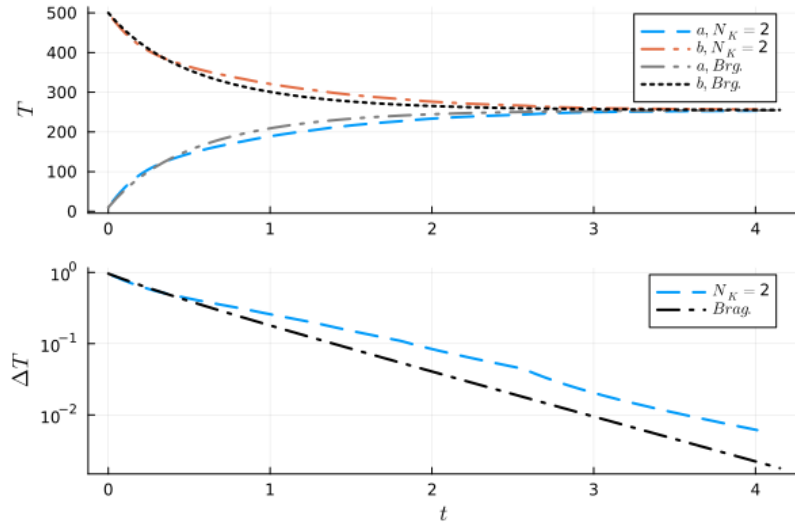


Figure 13: Two-species temperature equilibration with temperatures,  $T_a = 10$ ,  $T_b = 500$  and fixed timestep,  $\Delta t = 2^{-5}$ : When  $N_K = 2$  and  $(n_2, N_0) = (8, 7)$ .

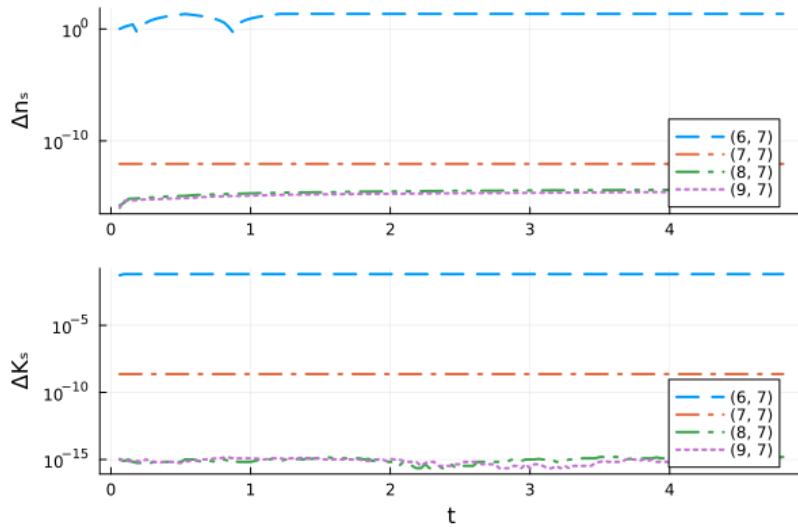


Figure 14: Two-species temperature equilibration with temperatures,  $T_a = 10$ ,  $T_b = 500$  and fixed timestep,  $\Delta t = 2^{-5}$ : Discrete conservation errors as functions of time and  $n_2$  when  $N_0 = 7$ .

## 5.2 Electron-Deuterium thermal equilibration

In order to verify the convergence in scenarios involving significant mass disparity, we examine  $e$ - $D$  temperature equilibration with parameters  $m_e = 1/1836$ ,  $m_D = 2$ ,  $-Z_e = Z_D = 1$ ,  $n_e = n_D = 1$ ,  $\hat{u}_e = \hat{u}_D = 0$ ,  $T_e = 1$  and  $T_D = 10$ . In this instance, the final average velocity and temperatures of the thermal equilibrium state are expected to be  $u_\infty = 0$  and  $T_\infty = 5.5$  respectively. The L01jd2 scheme is employed for solving this case with a self-adaptive timestep. The total number of timestep, denoted as  $N_t$ , is 792, when the termination condition is  $\Delta s_s \leq 10^{-8}$ . We aim to demonstrate that L01jd2 scheme provides a reliable approximation of the fully kinetic model for situations characterized by large mass disparity.

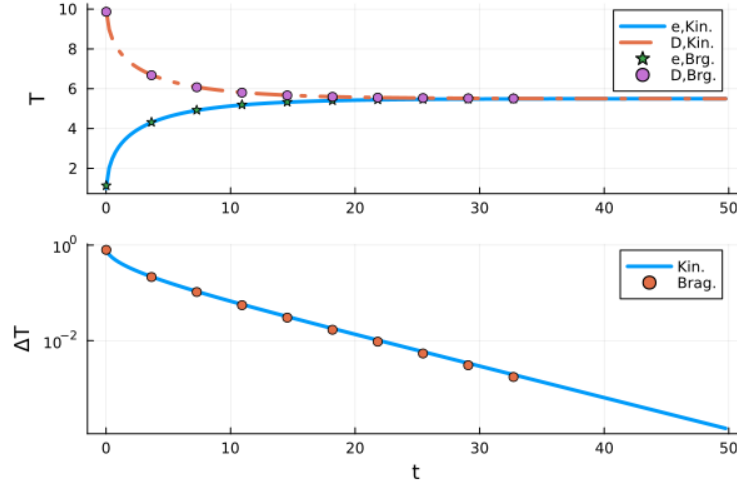


Figure 15:  $e$ - $D$  thermal equilibration with enforcing conservation when solved by L01jd2 with fixed timestep,  $\Delta t = 2^{-5}$ : Average velocities and temperatures as function of time  $t$  when  $(n_2, N_0) = (7, 7)$ .

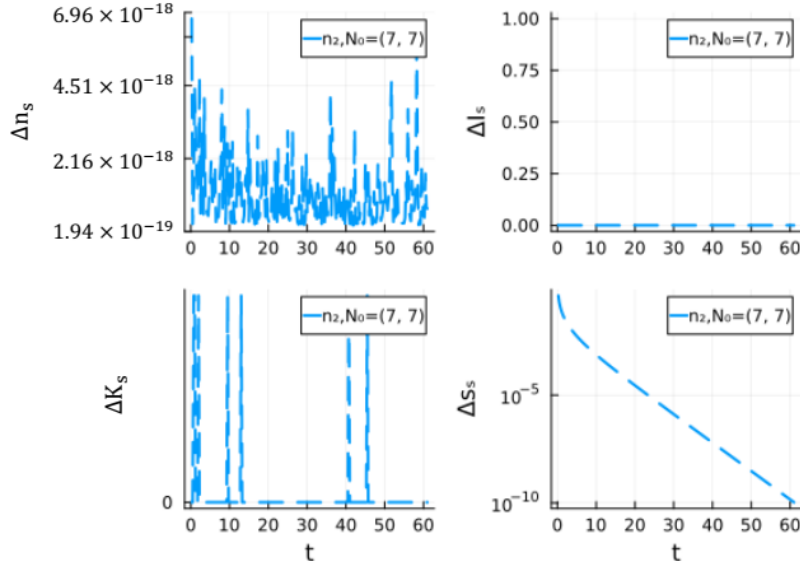


Figure 16:  $e$ - $D$  thermal equilibration with enforcing conservation when solved by L01jd2 with fixed timestep,  $\Delta t = 2^{-5}$ : Discrete conservation errors as functions of time when  $(n_2, N_0) = (7, 7)$ .

The temperatures of species  $e$  and  $D$  are presented as functions of time  $t$  in Fig. 15, demonstrating the attainment of correct equilibrium values. The temporal evolution of errors in discrete number density, momentum, energy conservation (113)-(115) and entropy conservation is illustrated in Fig. 16. Additionally, the local relative errors,  $Error(\delta_t \hat{n})$  and  $Error(\delta_t \hat{K})$  of species  $e$  and  $D$  are depicted in Fig. 17 when enforcing conservation. It can be observed that all errors of species  $D$  are at the level of round-off errors, which those for species  $e$  are acceptably small, aligning with the convergence criterion for conservation (give in Eq. (89)).

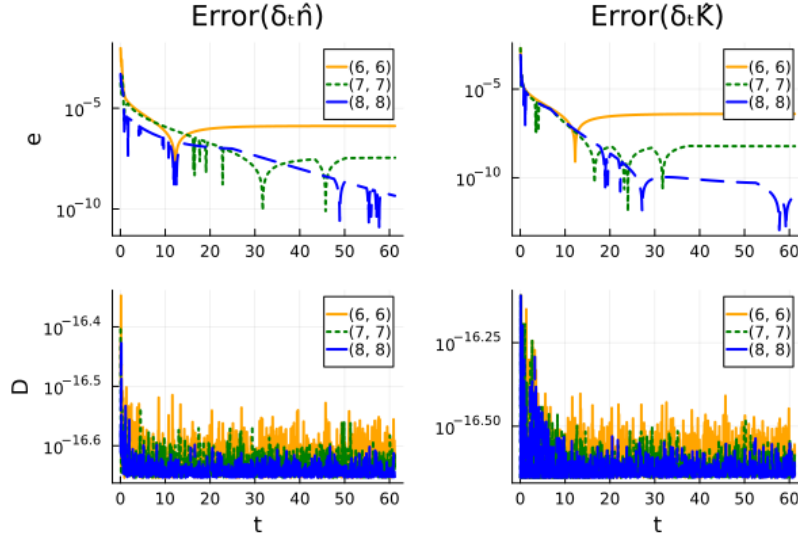


Figure 17:  $e$ - $D$  thermal equilibration with enforcing conservation when solved by L01jd2 with fixed timestep,  $\Delta t = 2^{-5}$ : Local errors of  $\delta_t \hat{n}$  and  $\delta_t \hat{K}$  as functions of time with various  $(n_2, N_0)$ .

To assess the effectiveness of L01jd2 in scenarios involving significant mass disparity, we validate its convergence with the following criterion:

$$\Delta_0 f_l(\hat{v}_\alpha, t_{k+1}) = |f_l^*(\hat{v}_\alpha, t_{k+1}) - f_l(\hat{v}_\alpha, t_{k+1})| / |f_l^*(\hat{v}_\alpha, t_{k+1}) - f_l(\hat{v}_\alpha, t_k)| = C_0. \quad (121)$$

and

$$\Delta_2 f_l = (N_v)^{-1} \sum_{\alpha=1}^{N_v} \delta f_l(\hat{v}_\alpha, t_{k+1}). \quad (122)$$

Here,

$$\delta f_l(\hat{v}_\alpha, t_{k+1}) = |f_l^*(\hat{v}_\alpha, t_{k+1}) - f_l(\hat{v}_\alpha, t_{k+1})| / |\Delta t \times f_l^*(\hat{v}_\alpha, t_{k+1})| = C_2(\Delta t)^2. \quad (123)$$

The functions  $f_l^*(\hat{v}, t_{k+1})$  and  $f_l(\hat{v}, t_{k+1})$  represent the  $l^{th}$ -order amplitude of distribution function before and after being smoothed by the King method at the  $(k+1)^{th}$  timestep for species  $a$ , respectively.

The convergence of function  $\Delta_2 f_l$  is illustrated in Fig. 18, with a fixed final time of  $t_{k+1} = 0.5$ . The right-lower subplot in Fig. 18 presents compelling evidence of the second-order accuracy convergence of King method as  $\Delta t$  is refined. When using a sufficiently small timestep, such as  $\Delta t = 0.01$ , the maximum relative disparity of the distribution function before and after being smoothed by the King method does not exceed 11% for species  $e$  and  $10^{-5}$  for species  $D$  in this scenario. This can be observed from the

distribution function at  $k^{th}$  and  $(k + 1)^{th}$  time steps for species  $e$  and  $D$  in Fig. 18 (upper). The detailed relative disparity as a function of  $\hat{v}$  is plotted in the left-lower subplot of Fig. 18 when  $\Delta t = 2^{-5}$ .

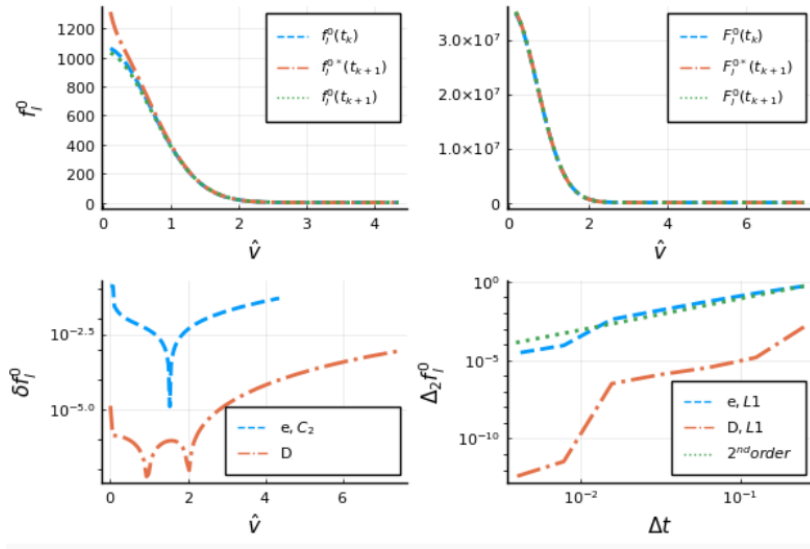


Figure 18: e-D temperature equilibration with enforcing conservation when solved by L01jd2 with fixed timestep,  $\Delta t = 2^{-5}$ : Criterion  $C_2$  (122) for situation with large mass disparity.

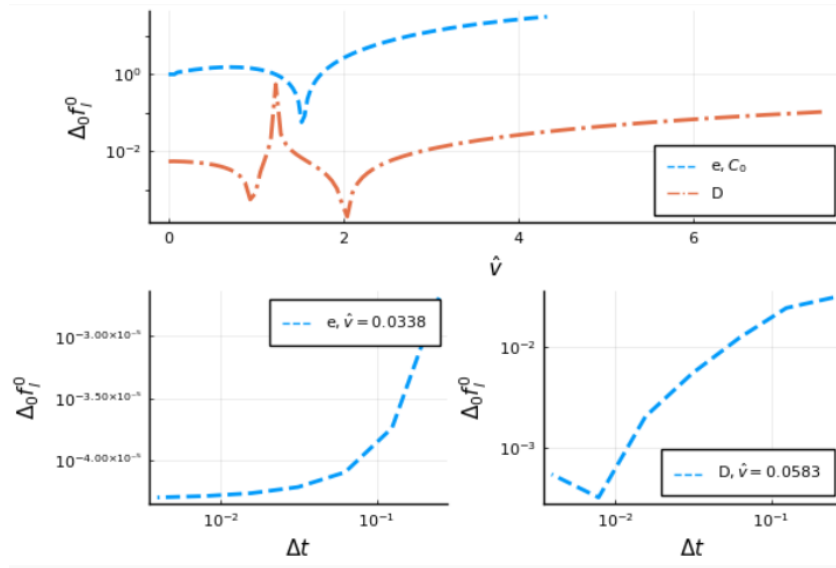


Figure 19: e-D temperature equilibration with enforcing conservation when solved by L01jd2 with fixed timestep,  $\Delta t = 2^{-5}$ : Criterion  $C_0$  (121) for situation with large mass disparity.

Similarly, the convergence of function  $\Delta_0 f_i$  at the grid point  $v_\alpha = 1.68 \times 10^{-2}$  is demonstrated in Fig. 19. The lower subplots show that the parameter  $C_0$  tends to stabilize as a constant with the refinement of  $\Delta t$  at single speed node, i.e.  $\hat{v}_\alpha = 0.0338$  for species  $e$  and  $\hat{v}_\alpha = 0.0583$  for species  $D$ . For species  $D$ , which exhibits a higher precision of distribution function,  $\Delta_0 f_i(\hat{v}_\alpha = 0.0583)$  remains bellows 0.1 for all provided timesteps and does not



exceed 1% when  $\Delta t = 2^{-5}$ . Considering the high precision of conservation in discrete with a acceptable timestep  $\Delta t = 2^{-5}$ , the L01jd2 scheme is a good approximation of the fully kinetic model for situations with large mass disparity.

### 5.3 Electron-Deuterium temperature and momentum equilibration

We consider  $e$ - $D$  temperature and momentum equilibration with parameters  $m_e = 1/1836$ ,  $m_D = 2$ ,  $-Z_e = Z_D = 1$ ,  $n_e = n_D = 1$ ,  $\hat{u}_e = 0.1$ ,  $\hat{u}_D = -3.162 \times 10^{-2}$ ,  $T_e = 1$  and  $T_D = 100$  when  $(n_2, N_0) = (7, 7)$ . The initial value of  $l_{M_1} = 13$ ,  $v_{eth} \approx 0.063$  and  $v_{Dth} \approx 0.010$ . The expected final average velocity and temperatures are approximately  $u_\infty \approx -9.769 \times 10^{-2}$  and  $T_\infty \approx 50.504$ , respectively. This case will also be solved by the L01jd2 scheme with a self-adaptive timestep, where the number of timestep is determined to be  $N_t = 4877$ . In theory, electron-deuterium momentum equilibration will occur first followed by reaching a state of temperature equilibration.

The average velocities and temperatures of species  $e$  and  $D$  are depicted as functions of time  $t$  in Fig. 20. The lens in Fig. 20 demonstrates that correct equilibrium values of momentum and temperature are achieved. As anticipated, the characteristic time for momentum relaxation time is significantly shorter than the characteristic time for temperature relaxation during the process of electron-deuterium temperature and momentum equilibration.

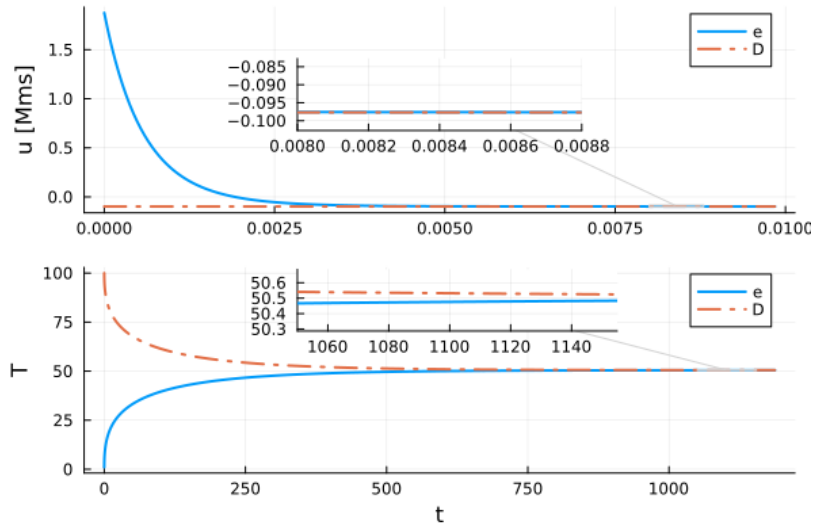


Figure 20:  $e$ - $D$  thermal and momentum equilibration with enforcing conservation: Average velocities and temperatures as function of time  $t$  when  $(n_2, N_0) = (7, 7)$ .

The time histories of the errors in discrete number density, momentum, energy conservation and entropy conservation are depicted in Fig. 21. As before, mass, momentum and energy conservation (113)-(115) are enforced to the level of round-off error and H-theorem are preserved all the time, as demonstrated in Fig. 21. Fig. 22 illustrates that the local relative errors,  $Error(\delta_t \hat{n})$ ,  $Error(\delta_t \hat{I})$ , and  $Error(\delta_t \hat{K})$  are sufficiently small, satisfying the convergence criterion for conservation (89) during  $e$ - $D$  collision when  $(n_2, N_0) = (7, 7)$ . As expected, the local relative errors of species  $D$ , with its larger mass, are smaller than those of species  $e$ . The convergence criterion  $\delta_t \hat{T}$  (displayed in Eq. (50)) is approximately valid with high precision, especially when  $t \geq 10^{-2}$ .

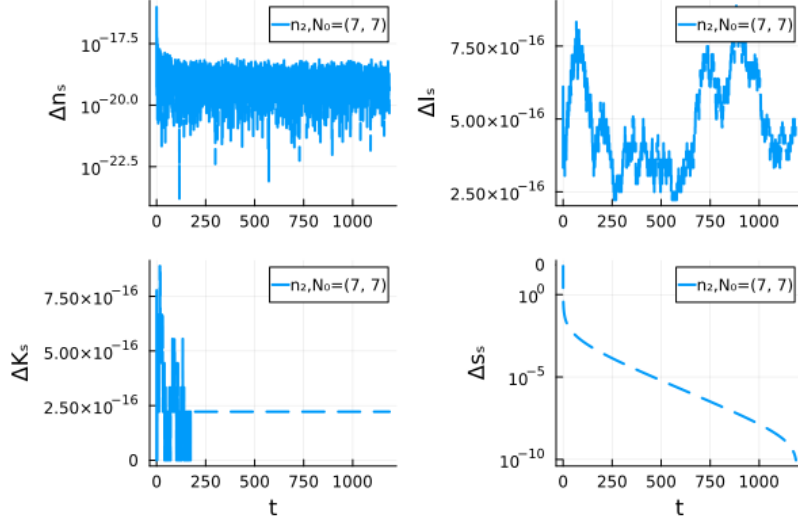


Figure 21:  $e$ - $D$  thermal and momentum equilibration with enforcing conservation when  $T_e = 1$  and  $T_D = 100$ : Discrete conservation errors as functions of time when  $(n_2, N_0) = (7, 7)$ .

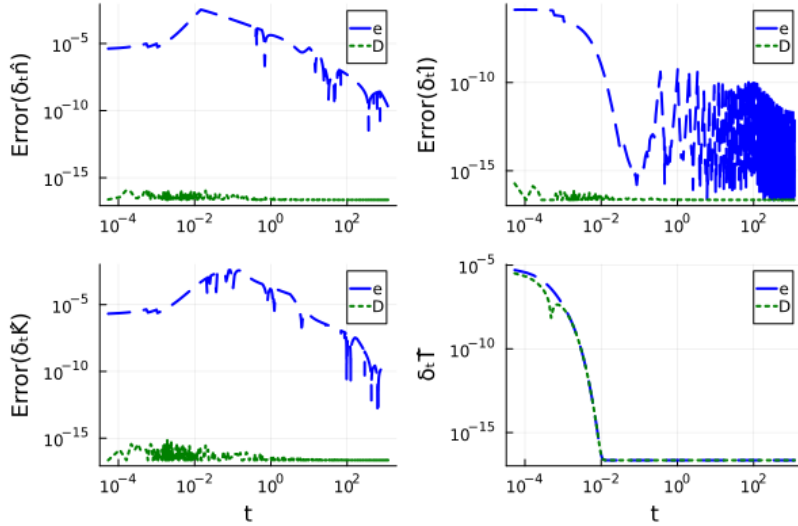


Figure 22:  $e$ - $D$  thermal and momentum equilibration with enforcing conservation when  $T_e = 1$  and  $T_D = 100$ : Local errors of  $\delta_t \hat{n}$ ,  $\delta_t \hat{I}$ ,  $\delta_t \hat{K}$  and convergence criterion  $\delta_t \hat{T}$  as functions of time when  $(n_2, N_0) = (7, 7)$ .

#### 5.4 Three-species ( $e$ - $D$ - $\alpha$ ) thermal equilibration

The final test case involves the three-species ( $e$ - $D$ - $\alpha$ ) thermal equilibration, which is an crucial issue in fusion plasma. Theoretically, the high-energy  $\alpha$  particles in burning plasma will initially exchange energy with electrons (of comparable  $v_{th}$ ) and later thermalize with  $D$  particles. The simulation parameters are  $m_e = 1/1836$ ,  $m_D = 2$ ,  $m_\alpha = 4$ ,  $-Z_e = Z_D = 1$ ,  $Z_\alpha = 2$ ,  $n_e = 3$ ,  $n_D = 1$ ,  $n_\alpha = 1$ . Initially  $\hat{u}_e = \hat{u}_D = \hat{u}_\alpha = 0$ ,  $T_e = T_D = 1$  and  $T_\alpha = 1750$ , we choose  $(n_2, N_0) = (7, 7)$ . In this case,  $v_{eth} \approx 6.256 \times 10^{-2}$ ,  $v_{Dth} \approx 1.036 \times 10^{-3}$  and  $v_{\alpha th} \approx 3.065 \times 10^{-2}$ . The characteristic time  $\tau_0$  is equivalent to the

initial temperature relaxation time between  $e$  and  $D$ ,  $\tau_0 = 1/\nu_T^{eD}$  where

$$\nu_T^{eD} \approx 441.72 \times \frac{\sqrt{m_e m_D} (Z_e Z_D)^2 n_D}{(m_e T_D + m_D T_e)^{3/2}} \ln \Lambda_{eD}. \quad (124)$$

The maximum thermal velocity ratio,  $v_{eth}/v_{Dth} \sim 60$ .

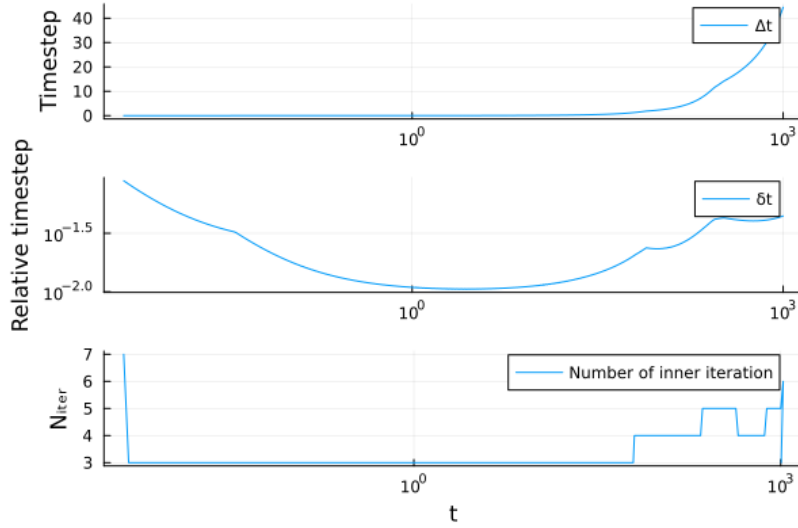


Figure 23:  $e$ - $D$ - $\alpha$  thermal equilibration: timestep  $\Delta t$ , the relative timestep  $\delta t$  and number of inner iteration  $N_{iter}$  as functions of time.

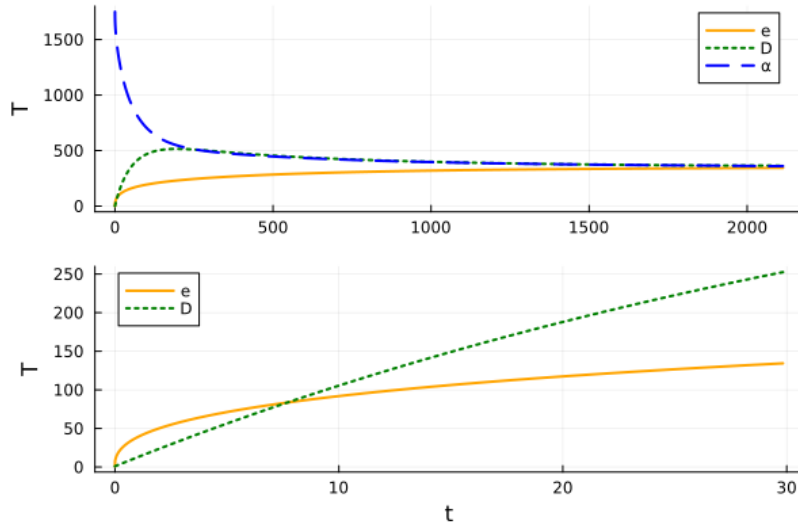


Figure 24:  $e$ - $D$ - $\alpha$  thermal equilibration: Temperature of the three species as functions of time (upper) and of  $e$  and  $D$  at the early time (lower).

This case is solved using a self-adaptive timesteps, with a total of 710 time levels. Fig. 23 illustrates the timestep  $\Delta t$ , the relative timestep  $\delta t$  and number of inner iteration  $N_{iter}$  as functions of time. Here, the  $k^{th}$  timestep and relative timestep are respectively

defined as  $\Delta t_k = t_{k+1} - t_k$  and  $\delta t_k = \Delta t_k / t_{k+1}$ . The number of inner iterations consistently remains below 10, regardless of the timestep and relative timestep. Additionally, due to the effectiveness of the King method, the value of  $N_{iter}$  typically does not exceed 5 in most time intervals.

The temperatures of all species as functions of time  $t$  are plotted in Fig. 24. As anticipated, the electrons exhibit a more rapid heating rate comparing to the  $D$  particles during the early stage when  $t \leq 8$  (lower figure in Fig. 24). However, as electrons and  $D$  quickly heat up while  $\alpha$  particles cool down, the preferential interaction switches to one between  $\alpha$  and  $D$ , ultimately leading to their thermalization together. Eventually, all three species reach the expected equilibrium temperature of  $T_\infty = 350.08$  (upper panel in Fig. 24).

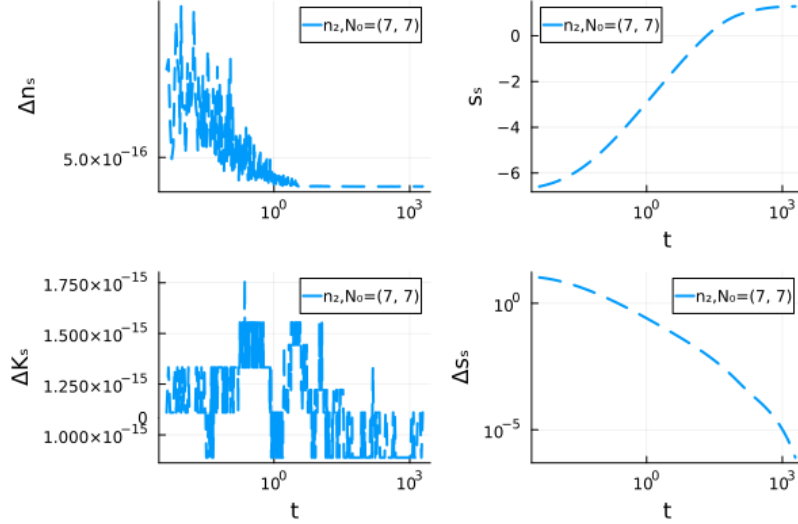


Figure 25:  $e$ - $D$ - $\alpha$  thermal equilibration: Discrete conservation errors as functions of time.

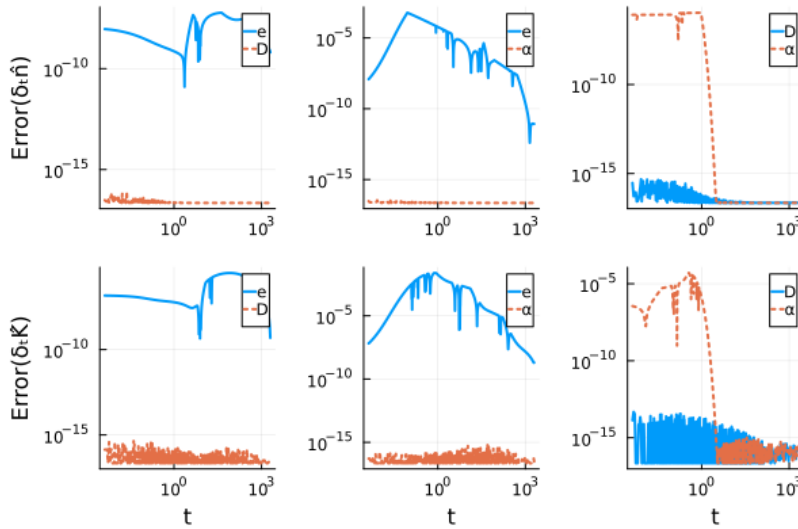


Figure 26:  $e$ - $D$ - $\alpha$  thermal equilibration: Local relative errors of  $\delta_t \hat{n}$  and  $\delta_t \hat{K}$  during all the two-species collision processes as functions of time.

The temporal histories of local errors in discrete number density, momentum, energy conservation and entropy conservation are plotted in Fig. 25. As expected, mass and energy conservation represented by Eq. (113) and Eq. (115) are enforced to the level of round-off error. The right-upper subplot of Fig. 25 demonstrates that the entropy satisfies the H-theorem at all time.  $\Delta s_s$  (116) is consistently non-negative, as showed in the right-lower subplot of Fig. 25. In this case, the value of  $\delta s_s$  is about  $-7.87$ . The total local relative errors of  $\delta_t \hat{n}$  and  $\delta_t \hat{K}$  for all species as functions of time  $t$  are presented in Fig. 26. It can be observed that the convergence criterion for conservation denoted by Eq. (89) is also satisfied for all sub-processes involving two-species collision process.

## 6 Conclusion

In this study, we have developed an implicit algorithm for solving the multi-species nonlinear 0D-2V axisymmetric Fokker-Planck-Rosenbluth collision equation based on the Shkarofsky's formula. The algorithm ensures mass, momentum, energy conservation and satisfies the H-theorem for general mass, temperature when average velocities are moderate. We construct an efficient algorithm based on the nonlinear Shkarofsky's formula of FPR (FPRS) collision operator. Legendre polynomial expansion is employed in the angular direction, which converges exponentially with the increment of number of the polynomials. King function expansion, a moment convergence method, is utilized in speed coordinate. The kinetic moments will be computed by Romberg integration with high precision. Post-step projection to manifold method is used to enforce exact conservation of the collision operators.

The high accuracy of our algorithm is demonstrated by solving several typical problems in various non-equilibrium configurations. To handle the large disparate of thermal velocities resulting from the arbitrary disparity of mass and temperature, we incorporate mapping between the different field nodes for collision species, which is also based on the King function. The fast convergence and high efficiency in handling various challenging problems have showcased the potential of our approach for multi-scale simulation of plasma.

In order to fully realize the potential of the proposed approach for nonlinear, multi-scale plasma systems, it is necessary to expand our approach into a general self-adaptive scheme with self-adaptive field nodes, which will be discussed in a future publication. We finally remark that the present approach (SHE together with KFE) is efficient for sub-sonic plasma system, while the L01jd2NK scheme is only designed for system without distinguishing asymmetries in velocity space, such as when  $\hat{u}_a \ll 1$ . The first reason for this limitation is that the decreasing convergence rate of SHE as the average velocity to thermal velocity ratio increases. For example,  $l = 3$  when  $\hat{u}_a \leq 2.2 \times 10^{-3}$  while  $l = 11$  when  $\hat{u}_a = 0.44$ . The second reason is that characteristic parameter in the King function (54) may depend on  $l$  when  $\hat{u}_a$  is large enough and tends to be 1, which is still under development.

## 7 Acknowledgments

We express our gratitude to Peifeng Fan and Bojing Zhu for their valuable discussions. We particularly appreciate the assistance of Shichao Wu and Ye Zhu in enhancing the English language of our manuscript. This work is supported by the GuangHe Foundation (ghfund202202018672), Collaborative Innovation Program of Hefei Science Center, CAS, (2021HSC-CIP019), National Magnetic Confinement Fusion Program of China (2019YFE03 060000), Director Funding of Hefei Institutes of Physical Science from Chi-

nese Academy of Sciences (Grant Nos. E25D0GZ5), and Geo-Algorithmic Plasma Simulator (GAPS) Project.

## Appendix A: King Function

When the velocity space exhibits axisymmetry with  $\hat{\mathbf{u}}_a = \hat{u}_a \mathbf{e}_z$ , the Gaussian function will be:

$$\mathcal{G}(\hat{v}, \mu) = \frac{\hat{n}_a}{\hat{v}_{ath}^3} e^{-[(\hat{v} - \hat{u}_a \mathbf{e}_z) / \hat{v}_{ath}]^2}. \quad (125)$$

The Gaussian function can be expanded using Legendre polynomials as:

$$\mathcal{G}(\hat{v}, \mu) = \sum_{l=0}^{\infty} \mathcal{G}_l(\hat{v}) P_l(\mu). \quad (126)$$

The  $l^{\text{th}}$ -order amplitude,  $\mathcal{G}_l(\hat{v})$  can be calculated by the inverse transformation of Eq. (126), reads:

$$\mathcal{G}_l(\hat{v}) = \int_{-1}^1 \mathcal{G}(\hat{v}, \mu) P_l(\mu) d\mu, \quad l \in 0, 1, \dots, l_M. \quad (127)$$

Substitute Eq. (125) into the equation above, and after a tedious derivation process, one can obtain:

$$\mathcal{G}_l(\hat{v}) = \frac{\hat{n}_a}{(\hat{v}_{ath})^3} \sum_{m=0}^l C_{G_l} \frac{1}{\hat{\xi}_a^{m+1}} \left[ (-1)^m e^{-\left(\frac{\hat{v}-\hat{u}_a}{\hat{v}_{ath}}\right)^2} - (-1)^l e^{-\left(\frac{\hat{v}+\hat{u}_a}{\hat{v}_{ath}}\right)^2} \right]. \quad (128)$$

Here,  $\hat{\xi}_a = 2\hat{v}\hat{u}_a/\hat{v}_{ath}^2$  and

$$C_{G_l} = \frac{2l+1}{2} \frac{1}{2^m m!} \frac{(l+m)!}{(l-m)!}. \quad (129)$$

The  $l^{\text{th}}$ -order King function (54) is in direct proportion to  $\mathcal{G}_l$ , reads:

$$\mathcal{K}_l(\hat{v}; \hat{u}_a, \hat{v}_{ath}) = \sqrt{\frac{1}{2\pi}} \frac{1}{\hat{n}_a} \mathcal{G}_l(\hat{v}). \quad (130)$$

The new function introduced in Sec. 3.2.1, King function (54) has the following properties. When  $v \rightarrow \infty$ , the King function will be:

$$\lim_{v \rightarrow \infty} \mathcal{K}_l(v; \iota, \sigma) \rightarrow 0. \quad (131)$$

When  $\xi = 2\iota v / \sigma^2 \rightarrow 0$ , the King function has the following asymptotic behaviour:

$$\lim_{\xi \rightarrow 0} \mathcal{K}_l(v; \iota, \sigma) = \sqrt{\frac{1}{2\pi}} \frac{e^{-\sigma^{-2}(v^2 + \iota^2)}}{(2l-1)!!} \frac{\xi^l}{\sigma^3} \left[ 1 + \sum_{k=1}^{\infty} \frac{1}{2^k k!} \frac{(2l-1)!!}{(2l+2k+1)!!} \xi^{2k} \right]. \quad (132)$$

In particular,  $\xi \equiv 0$  gives:

$$\mathcal{K}_l(v; \iota, \sigma) \stackrel{\xi=0}{=} \delta_l^0 \sqrt{\frac{1}{2\pi}} \frac{1}{\sigma^3} e^{-\sigma^{-2}(v^2 + \iota^2)}. \quad (133)$$

Here,  $\delta_l^0$  is the Kronecker symbol.

## Appendix B: Normalized FPRS collision operator

Substituting the distribution function (20), amplitudes of distribution function(21), (31) and amplitudes of Rosenbluth potentials (27)-(34) into the normalized FPRS collision operator (16), simplifying the result by combining the like terms yields the normalized FPRS collision operator in axisymmetric velocity space, reads:

$$\hat{\mathcal{C}}_{ab}(\hat{\mathbf{v}}, t) = 4\pi \sum_{i=0}^9 \hat{\mathcal{S}}_i. \quad (134)$$

The zero-order effect term resulting from  $\hat{F}$  in the collision term can be formulated as:

$$\hat{\mathcal{S}}_0 = m_M \sum_{L=0}^{\infty} \hat{F}_L(\hat{v}_{ab}, t) P_L \times \sum_{l=0}^{\infty} \hat{f}_l(\hat{v}, t) P_l. \quad (135)$$

The first-order effect terms resulting from  $\hat{H}_L$  will be:

$$\hat{\mathcal{S}}_1 = C_{\hat{H}} \sum_{L=0}^{\infty} P_L \frac{\partial}{\partial \hat{v}_{ab}} \hat{H}_L \times \sum_{l=0}^{\infty} P_l \frac{\partial}{\partial \hat{v}} \hat{f}_l, \quad (136)$$

$$\hat{\mathcal{S}}_2 = C_{\hat{H}} \frac{1}{\hat{v}_{ab}} \sum_{L=1}^{\infty} \hat{H}_L P_L^1 \times \frac{1}{\hat{v}} \sum_{l=1}^{\infty} \hat{f}_l P_l^1. \quad (137)$$

Another first-order effect term,  $\hat{\mathcal{S}}_3$ , will be zero due to the azimuthal derivatives is zero. Specifically, when  $m_a = m_b$ , the coefficient  $C_{\hat{H}} \equiv 0$ , resulting in  $\hat{\mathcal{S}}_1 = \hat{\mathcal{S}}_2 \equiv 0$  as well. Similarly, the second-order effect terms related to  $\hat{G}_L$  will be:

$$\hat{\mathcal{S}}_4 = C_{\hat{G}} \sum_{L=0}^{\infty} P_L \frac{\partial^2}{\partial \hat{v}_{ab}^2} \hat{G}_L \times \sum_{l=0}^{\infty} P_l \frac{\partial^2}{\partial \hat{v}^2} \hat{f}_l, \quad (138)$$

$$\hat{\mathcal{S}}_5 = 2C_{\hat{G}} \frac{1}{\hat{v}_{ab}} \sum_{L=1}^{\infty} \left( \frac{\hat{G}_L}{\hat{v}_{ab}} - P_L \frac{\partial}{\partial \hat{v}_{ab}} \hat{G}_L \right) \times \frac{1}{\hat{v}} \sum_{l=1}^{\infty} \left( \frac{\hat{f}_l}{\hat{v}} - P_l \frac{\partial}{\partial \hat{v}} \hat{f}_l \right) P_l^1, \quad (139)$$

$$\hat{\mathcal{S}}_7 = C_{\hat{G}} \frac{1}{\hat{v}_{ab}} \sum_{L=0}^{\infty} \left( P_L^{1,2} \frac{\hat{G}_L}{\hat{v}_{ab}} + P_L \frac{\partial \hat{G}_L}{\partial \hat{v}_{ab}} \right) \times \frac{1}{\hat{v}} \sum_{l=0}^{\infty} \left( P_l^{1,2} \frac{\hat{f}_l}{\hat{v}} + P_l \frac{\partial \hat{f}_l}{\partial \hat{v}} \right), \quad (140)$$

$$\hat{\mathcal{S}}_9 = C_{\hat{G}} \sum_{L=0}^{\infty} \left( P_L^{1,\mu} \frac{\hat{G}_L}{\hat{v}_{ab}^2} + P_L \frac{1}{\hat{v}_{ab}} \frac{\partial \hat{G}_L}{\partial \hat{v}_{ab}} \right) \times \sum_{l=0}^{\infty} \left( P_l^{1,\mu} \frac{\hat{f}_l}{\hat{v}^2} + P_l \frac{1}{\hat{v}} \frac{\partial \hat{f}_l}{\partial \hat{v}} \right), \quad (141)$$

where

$$P_l^{1,\mu} = \frac{\mu}{\sqrt{1-\mu^2}} P_l^1, \quad (142)$$

$$P_l^{1,2} = P_l^2 + P_l^{1,\mu}. \quad (143)$$

The remaining second-order effect terms vanish,  $\hat{\mathcal{S}}_6 = \hat{\mathcal{S}}_8 = 0$ . As demonstrated by the equations above, the FPRS collision operator (give in Eq. (134)) is generally a nonlinear

model.

In particular, when the system is spherical symmetric in velocity space, the collision effect becomes independent of the angular direction of velocity space. Therefore, the normalized FPRS collision operator (give in Eq. (134)) will be:

$$\hat{\mathcal{S}}_0(\hat{\mathbf{v}}, t) = m_M \hat{F}_0(\hat{v}_{ab}, t) \times \hat{f}_0(\hat{v}, t), \quad (144)$$

$$\hat{\mathcal{S}}_1(\hat{\mathbf{v}}, t) = C_{\hat{H}} \frac{\partial}{\partial \hat{v}_{ab}} \hat{H}_0 \times \frac{\partial}{\partial \hat{v}} \hat{f}_0, \quad (145)$$

$$\hat{\mathcal{S}}_4(\hat{\mathbf{v}}, t) = C_{\hat{G}} \frac{\partial^2}{\partial \hat{v}_{ab}^2} \hat{G}_0 \times \frac{\partial^2}{\partial \hat{v}^2} \hat{f}_0, \quad (146)$$

$$\hat{\mathcal{S}}_7(\hat{\mathbf{v}}, t) = \hat{\mathcal{S}}_9 = C_{\hat{G}} \frac{1}{\hat{v}_{ab}} \frac{\partial}{\partial \hat{v}_{ab}} \hat{G}_0 \times \frac{1}{\hat{v}} \frac{\partial}{\partial \hat{v}} \hat{f}_0. \quad (147)$$

The remaining first-order effect terms and second-order effect terms will be zero,  $\hat{\mathcal{S}}_2 = \hat{\mathcal{S}}_3 = \hat{\mathcal{S}}_5 = \hat{\mathcal{S}}_6 = \hat{\mathcal{S}}_8 = 0$ .

For self-collision process where  $m_M = 1$ , the coefficients (give in Eq. (17)) will remain constants, reads:

$$C_{\hat{F}} = 4\pi, \quad C_{\hat{H}} = 0, \quad C_{\hat{G}} = 1/2. \quad (148)$$

The normalized FPRS collision operator (give in Eqs. (134)-(147)) can be further simplify to a self-collision operator by substituting  $\hat{F}_L$  and  $\hat{v}_{ab}$  with  $\hat{f}_l$  and  $\hat{v}$  respectively.

## References

- [1] M. N. Rosenbluth, W. M. MacDonald, and D. L. Judd, "Fokker-planck equation for an inverse-square force," *Physical Review*, vol. 107, no. 1, pp. 1–6, 1957.
- [2] W. T. Taitano, L. Chacón, A. N. Simakov, and K. Molvig, "A mass, momentum, and energy conserving, fully implicit, scalable algorithm for the multi-dimensional, multi-species Rosenbluth-Fokker-Planck equation," *Journal of Computational Physics*, vol. 297, pp. 357–380, 2015.
- [3] I. P. Shkarofsky, "Cartesian Tensor Expansion of the Fokker–Planck Equation," *Canadian Journal of Physics*, vol. 41, no. 11, pp. 1753–1775, 1963.
- [4] I. P. Shkarofsky, T. W. Johnston, M. P. Bachynski, and J. L. Hirshfield, "The Particle Kinetics of Plasmas," *American Journal of Physics*, vol. 35, pp. 551–552, 6 1967.
- [5] L. D. Landau, "The kinetic equation in the case of Coulomb interaction," *Zh. Eksper. i Theoret. Fiz.* 7 (2), 1937.
- [6] A. A. Vlasov, "THE VIBRATIONAL PROPERTIES OF AN ELECTRON GAS," *Soviet Physics Uspekhi*, vol. 10, pp. 721–733, 6 1968.
- [7] V. L. Boltzmann, "Weitere Studien uber das Warmegleichgewicht unter Gas-molekullen," *Wissenschaftliche Abhandlungen*, 1872.
- [8] J. Chang and G. Cooper, "A practical difference scheme for Fokker-Planck equations," *Journal of Computational Physics*, vol. 6, pp. 1–16, 8 1970.
- [9] W. T. Taitano, L. Chacón, and A. N. Simakov, "An adaptive, conservative 0D-2V multispecies Rosenbluth-Fokker-Planck solver for arbitrarily disparate mass and temperature regimes," *Journal of Computational Physics*, vol. 318, pp. 391–420, 2016.



- [10] A. G. Thomas, M. Tzoufras, A. P. Robinson, R. J. Kingham, C. P. Ridgers, M. Sherlock, and A. R. Bell, "A review of Vlasov-Fokker-Planck numerical modeling of inertial confinement fusion plasma," *Journal of Computational Physics*, vol. 231, no. 3, pp. 1051–1079, 2012.
- [11] A. R. Bell, A. P. Robinson, M. Sherlock, R. J. Kingham, and W. Rozmus, "Fast electron transport in laser-produced plasmas and the KALOS code for solution of the Vlasov-Fokker-Planck equation," *Plasma Physics and Controlled Fusion*, vol. 48, no. 3, 2006.
- [12] T. W. Johnston, "Cartesian tensor scalar product and spherical harmonic expansions in boltzmann's equation," *Physical Review*, vol. 120, no. 4, pp. 1103–1111, 1960.
- [13] I. P. Shkarofsky, "Expansion of the relativistic Fokker-Planck equation including non-linear terms and a non-Maxwellian background," *Physics of Plasmas*, vol. 4, no. 7, pp. 2464–2481, 1997.
- [14] R. J. Kingham and A. R. Bell, "An implicit Vlasov-Fokker-Planck code to model non-local electron transport in 2-D with magnetic fields," *Journal of Computational Physics*, vol. 194, no. 1, pp. 1–34, 2004.
- [15] A. G. Thomas, R. J. Kingham, and C. P. Ridgers, "Rapid self-magnetization of laser speckles in plasmas by nonlinear anisotropic instability," *New Journal of Physics*, vol. 11, 2009.
- [16] A. P. Robinson, M. Sherlock, and P. A. Norreys, "Artificial collimation of fast-electron beams with two laser pulses," *Physical Review Letters*, vol. 100, no. 2, pp. 1–4, 2008.
- [17] M. Tzoufras, A. R. Bell, P. A. Norreys, and F. S. Tsung, "A Vlasov-Fokker-Planck code for high energy density physics," *Journal of Computational Physics*, vol. 230, no. 17, pp. 6475–6494, 2011.
- [18] M. Tzoufras, A. Tableman, F. S. Tsung, W. B. Mori, and A. R. Bell, "A multi-dimensional Vlasov-Fokker-Planck code for arbitrarily anisotropic high-energy-density plasmas," *Physics of Plasmas*, vol. 20, no. 5, 2013.
- [19] S. Z. Wu, H. Zhang, C. T. Zhou, S. P. Zhu, and X. T. He, "Kinetic model for energy deposition in fast ignition," in *EPJ Web of Conferences*, vol. 59, 2013.
- [20] S. Mijin, F. Militello, S. Newton, J. Omotani, and R. J. Kingham, "Kinetic and fluid simulations of parallel electron transport during equilibria and transients in the scrape-off layer," *Plasma Physics and Controlled Fusion*, vol. 62, no. 9, 2020.
- [21] M. Krook and T. T. Wu, "Exact solutions of the Boltzmann equation," *Physics of Fluids*, vol. 20, no. 10, pp. 1589–1596, 1977.
- [22] A. R. Bell, R. G. Evans, and D. J. Nicholas, "Electron energy transport in steep temperature gradients in laser-produced plasmas," *Physical Review Letters*, vol. 46, no. 4, pp. 243–246, 1981.
- [23] J. P. Matte and J. Virmont, "Electron Heat Transport down Steep Temperature Gradients," *Physical Review Letters*, vol. 49, pp. 1936–1939, 12 1982.
- [24] I. P. Shkarofsky, M. M. Shoucri, and V. Fuchs, "Numerical solution of the Fokker-Planck equation with a dc electric field," *Computer Physics Communications*, vol. 71, no. 3, pp. 269–284, 1992.
- [25] F. Alouani-Bibi, M. M. Shoucri, and J. P. Matte, "Different Fokker-Planck approaches to simulate electron transport in plasmas," *Computer Physics Communications*, vol. 164, no. 1-3, pp. 60–66, 2004.
- [26] B. Zhao, G. Y. Hu, J. Zheng, and Y. Ding, "Simulations of nonlocal electron transport in cylindrical and spherical thermal waves," *High Energy Density Physics*, vol. 28, no. April, pp. 1–6, 2018.

- [27] S. Wu, C. Zhou, S. Zhu, H. Zhang, and X. He, "Relativistic kinetic model for energy deposition of intense laser-driven electrons in fast ignition scenario," *Physics of Plasmas*, vol. 18, 2 2011.
- [28] L. Pareschi, G. Russo, and G. Toscani, "Fast Spectral Methods for the Fokker-Planck-Landau Collision Operator," *Journal of Computational Physics*, vol. 165, no. 1, pp. 216–236, 2000.
- [29] F. Filbet and L. Pareschi, "A Numerical Method for the Accurate Solution of the Fokker-Planck-Landau Equation in the Nonhomogeneous Case," *Journal of Computational Physics*, vol. 179, pp. 1–26, 6 2002.
- [30] A. Pataki and L. Greengard, "Fast elliptic solvers in cylindrical coordinates and the Coulomb collision operator," *Journal of Computational Physics*, vol. 230, no. 21, pp. 7840–7852, 2011.
- [31] M. Askari and H. Adibi, "Meshless method for the numerical solution of the Fokker-Planck equation," *Ain Shams Engineering Journal*, vol. 6, pp. 1211–1216, 12 2015.
- [32] Morton K. W. and Mayyers David, *Numerical Solution of Partial Differential Equations*, vol. 54. Cambridge University Press, 2005.
- [33] R. Li, Y. Ren, and Y. Wang, "Hermite spectral method for Fokker-Planck-Landau equation modeling collisional plasma," *Journal of Computational Physics*, vol. 434, 6 2021.
- [34] W. H. Press, S. A. Teukolsky, W. T. Vetterling, and F. B. P., *Numerical Recipes*. No. 9, Cambridge University Press, 2007.
- [35] W. T. Taitano, D. A. Knoll, and L. Chacón, "Charge-and-energy conserving moment-based accelerator for a multi-species Vlasov-Fokker-Planck-Ampère system, part II: Collisional aspects," *Journal of Computational Physics*, vol. 284, pp. 737–757, 3 2015.
- [36] W. T. Taitano, L. Chacón, and A. N. Simakov, "An equilibrium-preserving discretization for the nonlinear Rosenbluth-Fokker-Planck operator in arbitrary multi-dimensional geometry," *Journal of Computational Physics*, vol. 339, pp. 453–460, 2017.
- [37] D. Daniel, W. T. Taitano, and L. Chacón, "A fully implicit, scalable, conservative nonlinear relativistic Fokker-Planck 0D-2P solver for runaway electrons," *Computer Physics Communications*, vol. 254, p. 107361, 2020.
- [38] R. Courant, K. Friedrichs, and H. Lewy, "Über die partiellen Differenzgleichungen der mathematischen Physik," in *Kurt Otto Friedrichs*, pp. 53–95, Boston, MA: Birkhäuser Boston, 1986.
- [39] Y. Saad, *Iterative Methods for Sparse Linear Systems, Second Edition*. Society for Industrial and Applied Mathematics, 2003.
- [40] O. Larroche, "Kinetic simulations of fuel ion transport in ICF target implosions," *The European Physical Journal D - Atomic, Molecular and Optical Physics*, vol. 27, pp. 131–146, 11 2003.
- [41] Hairer E., Wanner G., and Lubich C., *Geometric Numerical Integration*, vol. 31 of *Springer Series in Computational Mathematics*. Berlin/Heidelberg: Springer-Verlag, 2006.
- [42] B. Moore and S. Reich, "Backward error analysis for multi-symplectic integration methods," *Numerische Mathematik*, vol. 95, no. 4, pp. 625–652, 2003.
- [43] S. Reich, "Backward error analysis for numerical integrators," *SIAM Journal on Numerical Analysis*, vol. 36, no. 5, pp. 1549–1570, 1999.
- [44] G. Liu, *An Introduction to Meshfree Methods and Their Programming*. Springer-Verlag, 2005.

- [45] C. Rackauckas and Q. Nie, “DifferentialEquations.jl—a performant and feature-rich ecosystem for solving differential equations in Julia,” *Journal of Open Research Software*, vol. 5, no. 1, 2017.
- [46] F. L. Bauer, “Algorithm 60: Romberg integration,” *Communications of the ACM*, vol. 4, p. 255, 6 1961.
- [47] E. Hairer, “Backward error analysis for multistep methods,” *Numerische Mathematik*, vol. 84, no. 2, pp. 199–232, 1999.
- [48] J. D. Huba, *NRL PLASMA FORMULARY*. NRL, 2011.
- [49] S. I. Braginskii, “Transport Processes in a Plasma,” *Reviews of Plasma Physics*, vol. 1, p. 205, 1 1965.
- [50] R. E. Robson and K. F. Ness, “Velocity distribution function and transport coefficients of electron swarms in gases: Spherical-harmonics decomposition of Boltzmanns equation,” *Physical Review A*, vol. 33, no. 3, pp. 2068–2077, 1986.
- [51] A. Sunahara, J. A. Delettrez, C. Stoeckl, R. W. Short, and S. Skupsky, “Time-Dependent Electron Thermal Flux Inhibition in Direct-Drive Laser Implosions,” *Physical Review Letters*, vol. 91, no. 9, pp. 1–4, 2003.
- [52] A. S. Joglekar, B. J. Winjum, A. Tableman, H. Wen, M. Tzoufras, and W. B. Mori, “Validation of OSHUN against collisionless and collisional plasma physics,” *Plasma Physics and Controlled Fusion*, vol. 60, no. 6, 2018.
- [53] B. Fornberg, “Calculation of weights in finite difference formulas,” *SIAM Review*, vol. 40, no. 3, pp. 685–691, 1998.
- [54] Y. Wang, J. Xiao, X. Rao, P. Zhang, Y. Adil, and G. Zhuang, “Relaxation model for a homogeneous plasma with spherically symmetric velocity space,” 2024.
- [55] N. Wiener, “Tauberian theorems,” *The Annals of Mathematics*, vol. 33, p. 1, 1 1932.
- [56] D. C.-L. Fong and M. Saunders, “LSMR: An Iterative Algorithm for Sparse Least-Squares Problems,” *SIAM Journal on Scientific Computing*, vol. 33, pp. 2950–2971, 1 2011.
- [57] S. J. Wright and J. N. Holt, “An inexact Levenberg-Marquardt method for large sparse nonlinear least squares,” *The Journal of the Australian Mathematical Society. Series B. Applied Mathematics*, vol. 26, pp. 387–403, 4 1985.
- [58] C. Kanzow, N. Yamashita, and M. Fukushima, “Levenberg-Marquardt methods with strong local convergence properties for solving nonlinear equations with convex constraints,” *Journal of Computational and Applied Mathematics*, vol. 172, pp. 375–397, 12 2004.
- [59] S. I. Braginskii, “Transport phenomena in a completely ionized two-temperature plasma,” *J. Exptl. Theoret. Phys. (U.S.S.R.)*, vol. 6, no. 33, pp. 459–472, 1958.
- [60] B. Fornberg, *A Practical Guide to Pseudospectral Methods*. Cambridge University Press, 1 1996.